Global manifolds of saddle periodic orbits parametrised by isochrons

James Hannam, Bernd Krauskopf and Hinke M. Osinga
Department of Mathematics, The University of Auckland, Private Bag 92019, Auckland 1142, New Zealand

February 2023

Abstract

Global stable and unstable manifolds of a saddle periodic orbit of a vector field carry phase information of how trajectories on the manifold approach the periodic orbit in forward or backward time. This information is encoded on the respective manifold by its foliation by isochrons, which are submanifolds of codimension one comprising all points that are in asymptotic synchrony with a point of a given phase on the periodic orbit. We present a method that finds a two-dimensional stable or unstable manifold of a saddle periodic orbit by computing a representative number of one-dimensional isochrons as arclength-parametrised curves on the manifold. As is demonstrated with examples of both orientable and non-orientable manifolds, this computational approach allows us to determine and visualise the interplay between their topological, geometric as well as synchronisation properties.

When investigating a given physical system, one will most likely come across some form of oscillation. Commonly used models represent sustained and experientally observable oscillations by attracting periodic orbits of a system of ordinary differential equations (ODEs). In this context, the asymptotic phase of an observed oscillation relative to some reference will often be significant [7, 11, 32]. Phase behaviour of an oscillation is encoded in ODEs by the *isochrons*, which are curves or, more generally, (hyper-)surfaces of equal phase that foliate the basin of attraction of the respective periodic orbit; see the next section for their formal definition. In particular, the resynchronisation behaviour of the system following any external perturbation is encoded in the topological and geometric properties of the isochrons. The concepts of asymptotic phase and isochrons were introduced by Winfree [36, 37] in the 1970s in the application context of modeling biological oscillation, such as the circadian rhythm.

With the limited computational and visualisation capabilities of the time, Winfree realised that already in planar systems the geometry of the isochrons, which are curves in this case, may be very complicated. Specifically, he computed and then sketched such isochrons indirectly from computed asymptotic phases of points in the basin, which he found by computing trajectories that end sufficiently close to a chosen point on the periodic orbit. As Winfree demonstrated in [38], this indirect method is not able to resolve the isochrons as curves in regions of large phase sensitivity. This realisation is behind more recent methods that compute isochrons directly as curves when the system is of dimension two. One approach is to compute one-dimensional isochrons by extending, via integration in backward time, a first local approximation of a given isochron [2, 4, 12, 16, 30, 33, 34]. In the presence of strong phase sensitivity the globalisation of isochrons as curves via integration may still be challenging numerically. This motivated the alternative approach, taken here as well, of computing isochrons via setting up a one-parameter family of well-posed two-point boundary value problems (BVPs), one end point of which traces out the isochron associated with a given point on the periodic orbit. This BVP approach was introduced in [28] and refined in [22, 23] and [13, 14]. It allows one to compute one-dimensional

isochrons in planar systems reliably, efficiently and accurately — even in the presence of extreme phase sensitivity — as smooth curves parametrised by their arclength; see also [6, 19]. This has been demonstrated for periodic orbits as well as focus equilibria that are attracting or repelling, and we speak of their forward-time and backward-time isochrons, respectively. In fact, finding both forward-time and by backward-time isochrons in regions where they co-exist enables one to identify changes in the intersection properties of these two foliations that are associated with the emergence of phase sensitivity [13, 14, 22, 23].

Apart from attracting and repelling periodic orbits, one commonly encounters periodic orbits of saddle type in continuous-time dynamical systems with phase spaces of dimensions larger than two. Saddle periodic orbits have stable and unstable invariant manifolds, along which they are approached by trajectories in forward and backward time, respectively, and these are important objects for understanding the organisation of the overall dynamics. In particular, manifolds of codimension one act as separatrices of the flow that may form, for example, boundaries between different basins of attraction. These global manifolds cannot be found analytically and, hence, must be computed numerically. Already when it is of dimension two, it is a nontrivial task to compute and visualise a global invariant manifold. Several methods have been developed for this purpose, and they differ in how they represent a given two-dimensional stable or unstable manifold: for example, as a set of trajectory segments, a set of closed geodesics, as an invariant object of a PDE formulation, or as a set of covering boxes; see [18, 19] for overviews of the different computational approaches.

In this chapter we present a new way of computing and visualising the two-dimensional stable manifold $W^s(\Gamma^\times)$ and/or unstable manifold $W^u(\Gamma^\times)$ of a saddle-type periodic orbit $\Gamma^\times$ via their foliations by isochrons. These foliations not only represent $W^s(\Gamma^\times)$ and $W^u(\Gamma^\times)$ as surfaces but, in addition to their intrinsic geometric information, also encode information about phase sensitivity and the relative velocity of dynamics on these manifolds. In our implementation, the *isochron manifold algorithm*, we adapt the BVP approach for one-dimensional isochrons of planar system to this higher-dimensional context. To this end, we formulate a one-parameter family of BVPs whose solutions are orbit segments that lie both on $W^s(\Gamma^\times)$ or $W^u(\Gamma^\times)$ and have end points that both lie on the same isochron of a prescribed asymptotic phase θ. The key here is to define and compute a suitable fundamental segment that parametrises the family of orbit segments used to compute a specific isochron on the manifold; subsequently our algorithm proceeds effectively as for isochrons of a planar system. The presentation and implementation is for vector fields in $\mathbb{R}^3$, but it can also be used for systems in $\mathbb{R}^n$ with $n \geq 4$ as long as the manifold itself is of dimension two.

More specifically, we compute a sufficient number of isochrons on the respective manifold, which are uniformly distributed in phase and each computed up to a pre-specified maximal arclength L. From the computed set of phase-uniform isochrons we then generate a mesh on $W^s(\Gamma^\times)$ or $W^u(\Gamma^\times)$. This representation has the benefit of providing a natural two-dimensional parametrisation of the manifold in terms of the asymptotic phase θ and the arclength ℓ along its isochrons. In particular, the boundary of the computed part of the respective manifold lies at the chosen maximal arclength L along each computed isochron, and visualising the surface for increasing L allows us to 'grow the manifold along isochrons'. Indeed, the geometry of the isochrons provides clues to this phase dynamics on the global invariant manifolds $W^s(\Gamma^\times)$ and $W^u(\Gamma^\times)$ — globally and not just near $\Gamma^\times$. This allows us to illustrate the geometry of the two-dimensional invariant manifold as a surface and, at the same time, represent the synchronisation properties on it as the periodic orbit $\Gamma^\times$ is approached in forward or backward time. We demonstrate, with examples of both orientable and nonorientable manifolds, how this representation by isochron foliations can be used to visualise and gain insight into the interplay between the topological, geometric and synchronisation properties of global invariant manifolds of periodic orbits.

The chapter is organised as follows. Following the introduction of the necessary notation and definitions in Section 1, we present in Section 2 the formulation of the isochron manifold algorithm. Here the main focus in Section 2.1 is on finding the fundamental segment, and Section 2.3 then explains how the mesh is rendered from the set of computed isochrons. We proceed to demonstrate our method with three examples, where we make use of the phase information to render the computed surfaces in novel ways. In Section 3 we present a constructed model in $\mathbb{R}^3$ with explicitly defined manifold and isochron geometry, which allows it to serves as a test case for the isochron manifold algorithm. The next two examples concern two-dimensional manifolds in $\mathbb{R}^3$ whose geometry is not known beforehand. Firstly, in Section 4 we compute and show the foliation by isochrons of the orientable stable manifold of a saddle periodic orbit in the model by Sandstede from [29]. Secondly, in Section 5 we give an example of a nonorientable manifold of a saddle periodic orbit in the so-called ζ^3-model [3]. A first part of this manifold near the periodic orbit was computed and shown in [27]. We extend this computation here to explore the complicated geometry of this nonorientable manifold in a more global way, including how it relates to the geometry of the isochron foliation. We conclude in Section 6 with a brief summary and outlook.

1 Background and notation

We assume familiarity with the basic concepts of dynamical systems theory as they can be found in standard textbooks, such as [11, 21, 32], and focus here on additional notions and objects associated with phase and synchronisation. To set the stage, we consider throughout a sufficiently smooth (at least C^1) vector field

$$\frac{d\boldsymbol{x}}{dt} = \mathbf{F}(\boldsymbol{x}), \quad \boldsymbol{x} \in \mathbb{R}^n. \tag{1}$$

Generally, the function $\mathbf{F} : \mathbb{R}^n \to \mathbb{R}^n$ also depends on parameters, but we do not indicate this here for notational convenience. We denote by $\mathbf{\Phi}(t;\cdot)$ the flow

$$\begin{aligned} \mathbf{\Phi}(t;\cdot) : \mathbb{R}^n &\to \mathbb{R}^n \\ \boldsymbol{x} &\mapsto \mathbf{\Phi}(t;\boldsymbol{x}) \end{aligned} \tag{2}$$

of (1) over time $t \in \mathbb{R}^n$. Then the trajectory (or orbit) of (1) with initial condition $\boldsymbol{x_0} \in \mathbb{R}^n$ is given by

$$\boldsymbol{x}(t) = \mathbf{\Phi}(t;\boldsymbol{x_0}). \tag{3}$$

A periodic orbit Γ with period T_Γ is a closed trajectory given by

$$\Gamma := \{\mathbf{\Phi}(t;\gamma_0) \,|\, 0 \le t < T_\Gamma\} \tag{4}$$

with $\mathbf{\Phi}(T_\Gamma;\gamma_0) = \gamma_0$, where we assume that $T_\Gamma > 0$ is the smallest time with this property. Relative to the point $\gamma_0 \in \Gamma$, we construct a notion of phase

$$\theta = t/T_\Gamma \in [0,1). \tag{5}$$

By convention γ_0 is chosen to lie at the maximum with respect to the first coordinate along Γ. Note that, throughout, we define the phase θ to be from the interval $[0,1)$ (rather than the circle $\mathbb{S}^1$).

Suppose now that the periodic orbit $\Gamma = \Gamma^s$ is attracting, that is, all its Floquet multipliers have modulus smaller than 1, apart from the trivial Floquet multiplier at 1 corresponding to

the tangent direction to Γ^s. Then, following [36, 37, 38], the phase on Γ^s can be extended for all initial conditions $\boldsymbol{x_0}$ in its basin of attraction

$$\mathcal{A}(\Gamma^s) := \{\boldsymbol{x_0} \in \mathbb{R}^n \,|\, \boldsymbol{\Phi}(t; \boldsymbol{x_0}) \to \Gamma^s \text{ for } t \to \infty\} \tag{6}$$

to a notion of *asymptotic phase* $\Theta(\boldsymbol{x_0})$, given implicitly by

$$\lim_{t\to\infty} \|\boldsymbol{\Phi}(t; \boldsymbol{x_0}) - \boldsymbol{\Phi}(t + T_{\Gamma^s}\, \Theta(\boldsymbol{x_0}); \gamma_0)\| = 0, \tag{7}$$

where T_{Γ^s} is the period of Γ^s. For a given phase $\theta \in [0, 1)$ the isochron $I_\theta(\Gamma^s)$ of Γ^s consists of the initial conditions in $\mathcal{A}(\Gamma^s)$ that have identical asymptotic phase θ. Winfree [36, 37, 38] defines the isochrons as the level sets of the asymptotic phase function, given by

$$I_\theta(\Gamma^s) = \{\boldsymbol{x_0} \in \mathcal{A}(\Gamma^s) \,|\, \Theta(\boldsymbol{x}_0) = \theta\}. \tag{8}$$

Guckenheimer [10] offers the alternative interpretation that the isochron $I_\theta(\Gamma^s)$ is the stable manifold of the fixed point $\gamma_\theta \in \Gamma^s$ under the time-T_{Γ^s} map associated with the periodic orbit Γ^s. The Invariant Manifold Theorem [15] implies that the isochrons are $(n-1)$-dimensional smooth manifolds that are tangent to the linearisation of the time-T_{Γ^s} map at γ_θ. Moreover, any isochron $I_\phi(\Gamma^s)$ is the diffeomorphic image of a given $I_\theta(\Gamma^s)$ under the flow $\boldsymbol{\Phi}((\phi-\theta)T_{\Gamma^s}; \cdot)$. It follows that the isochrons $I_\theta(\Gamma^s)$ with $\theta \in [0, 1)$, which we refer to as the *forward-time isochrons* from now on, foliate the basin $\mathcal{A}(\Gamma^s)$; we denote this foliation

$$\mathcal{I}(\Gamma^s) := \{I_\theta(\Gamma^s) \,|\, \theta \in [0, 1)\}. \tag{9}$$

Suppose now that all non-trivial Floquet multipliers of a periodic orbit $\Gamma = \Gamma^u$ have modulus larger than 1, so that the periodic orbit is repelling. As was pointed out in [14, 23], asymptotic phase and isochrons for Γ^u can be defined entirely analogously in this case, simply by reversing time. Hence, the basin of repulsion

$$\mathcal{R}(\Gamma^u) := \{\boldsymbol{x_0} \in \mathbb{R}^n \,|\, \boldsymbol{\Phi}(t; \boldsymbol{x_0}) \to \Gamma^u \text{ for } t \to -\infty\} \tag{10}$$

is foliated by the *backward-time isochrons* $U_\theta(\Gamma^u)$ with $\theta \in [0, 1)$, which are the unstable manifolds of the fixed points $\gamma_\theta \in \Gamma^u$ under the time-T_{Γ^u} map; we denote this foliation

$$\mathcal{U}(\Gamma^u) := \{U_\theta(\Gamma^u) \,|\, \theta \in [0, 1)\}. \tag{11}$$

We now come to the central case of a periodic orbit $\Gamma = \Gamma^\times$ of saddle type, with non-trivial Floquet multipliers of both modulus less than 1 and modulus greater than 1. We further assume that there are no Floquet multipliers on the unit circle (apart from the trivial one), so that the periodic orbit is hyperbolic. Hence, $\Gamma^\times$ has, say, $k \geq 1$ attracting and $n - k - 1 \geq 1$ repelling directions. According to the Invariant Manifold Theorem for flows [11, 15, 21], the periodic orbit $\Gamma^\times$ has a stable invariant manifold

$$W^s(\Gamma^\times) = \{\boldsymbol{x_0} \in \mathbb{R}^n \,|\, \boldsymbol{\Phi}(t; \boldsymbol{x_0}) \to \Gamma^\times \text{ for } t \to \infty\} \tag{12}$$

of dimension k that is tangent to its stable Floquet bundle, and an unstable invariant manifold

$$W^u(\Gamma^\times) = \{\boldsymbol{x_0} \in \mathbb{R}^n \,|\, \boldsymbol{\Phi}(t; \boldsymbol{x_0}) \to \Gamma^\times \text{ for } t \to -\infty\} \tag{13}$$

of dimension $n-k-1$ that is tangent to its unstable Floquet bundle. Note that $\Gamma^\times \subseteq W^s(\Gamma^\times) \cup W^u(\Gamma^\times)$.

Clearly, trajectories on the stable manifold $W^s(\Gamma^\times)$ spiral towards $\Gamma^\times$ with a given phase. Since we can interpret $W^s(\Gamma^\times)$ as the basin of attraction of $\Gamma^\times$ when the flow is restricted to

$W^s(\Gamma^\times)$, we have that the stable manifold is foliated by forward-time isochrons $I_{\Gamma^\times}(\Gamma^\times)$ of the foliation

$$\mathcal{I}(\Gamma^\times) = W^s(\Gamma^\times). \tag{14}$$

Likewise the unstable manifold $W^u(\Gamma^\times)$, the basin of repulsion of $\Gamma^\times$ of the flow restricted to it, so it is foliated by backward-time isochrons $U_{\Gamma^\times}(\Gamma^\times)$ of the foliation

$$\mathcal{U}(\Gamma^\times) = W^u(\Gamma^\times). \tag{15}$$

Note that initial conditions $\boldsymbol{x_0} \in \mathbb{R}^n \setminus (W^s(\Gamma^\times) \cup W^u(\Gamma^\times))$ do not reach $\Gamma^\times$ in either forward or backward time, which means that the notions of asymptotic phase and isochron of a saddle periodic orbit is special and can only be defined on its stable and unstable manifolds.

The foliations provide a new way of considering and computing the invariant manifolds $W^s(\Gamma^\times)$ and $W^u(\Gamma^\times)$. In particular, this is the case when these manifolds are of dimension two, that is, surfaces, and the isochrons are curves. Since this is the direct generalisation of one-dimensional isochrons of stable and repelling periodic orbits of planar systems, the task is to adapt the known methods for their computation to ambient spaces of higher dimension. The isochron manifold algorithm introduced in the next section achieves exactly that for the refined BVP methods from [14].

2 Computing the isochron foliation of a two-dimensional invariant manifold

The planar BVP isochron algorithm from [14, 22, 28] computes one-dimensional isochrons as arclength-parametrised curves in a two-dimensional basin of attraction or repulsion. We now extend this approach, in the refined form presented in [14], to account for the further degrees of freedom available in a phase space of dimension larger than two. While this seems straightforward conceptually, careful consideration of the nature of two-dimensional invariant manifolds turns out to be important in this endeavour. We proceed by discussing the required BVP setup for the forward-time isochrons $I_\theta(\Gamma^\times)$ on the stable manifold $W^s(\Gamma^\times)$; backward-time isochrons $U_\theta(\Gamma^\times)$ of $W^u(\Gamma^\times)$ are computed in the same way by considering the vector field (1) with reversed time. For ease of exposition, the formulation is for vector fields in $\mathbb{R}^3$, but we do briefly discussed the more general case of computing a two-dimensional global manifold in $\mathbb{R}^n$ with $n > 3$.

The isochron manifold algorithm has been implemented within the continuation software package AUTO [5]. We remark that the formulation of the respective BVP in AUTO requires a rescaling of the vector field with the integration time, generally $T_{\Gamma^\times}$ in the present context, so that each orbit segment has its begin point at $t = 0$ and its end point at $t = 1$. For clarity of exposition, the algorithm is presented below not in its implemented form but in conceptual terms and without this rescaling.

2.1 Construction of the fundamental segment

The key idea behind our approach is to find for the given the point $\gamma_\theta \in \Gamma^\times$ a fundamental segment $\boldsymbol{s}_\theta$, which acts as an (approximate) fundamental domain. By this we mean that the orbit segments with end points on $\boldsymbol{s}_\theta$ after integration time $T_{\Gamma^\times}$ have the property that their begin points trace out an accurate numerical representation of (a first piece of) $I_\theta(\Gamma^\times)$. We focus here on the crucial new element compared to the planar case: the definition of the fundamental segment in $\mathbb{R}^3$ by making use of the two-dimensional linear information, as given by $\Gamma^\times$ and its stable Floquet vector $\boldsymbol{w}_\theta$ at γ_θ.

The periodic orbit $\Gamma^\times$ and associated stable Floquet bundle can be found with a standard BVP setup [20]. This can be done in such a way that $\Gamma^\times$ is represented by an orbit segment $\boldsymbol{\gamma}_\theta$ with integration time $T_{\Gamma^\times}$ subject to the combined periodicity and phase condition $\boldsymbol{\gamma}(0) = \boldsymbol{\gamma}(T_{\Gamma^\times}) = \gamma_\theta$; then the stable Floquet vector $\boldsymbol{w}_\theta$ (which we take to have unit length) at the point γ_θ is also readily available [14, 22, 24]. With $\boldsymbol{\gamma}_\theta$ and $\boldsymbol{w}_\theta$ as given input, we now define an orthonormal basis at γ_θ as follows. The stable eigenspace E^s_θ of $\Gamma^\times$ at γ_θ is spanned by $\boldsymbol{w}_\theta$ and $\mathbf{F}(\gamma_\theta)$, which is the Floquet vector at γ_θ of the trivial Floquet multiplier 1, given by the right-hand side of (1). We define $\boldsymbol{w}^{\boldsymbol{\Phi}}_\theta \in \operatorname{span}(\boldsymbol{w}_\theta, \mathbf{F}(\gamma_\theta))$ perpendicular to $\boldsymbol{w}_\theta$ by the orthonormalisation

$$\boldsymbol{w}^{\boldsymbol{\Phi}}_\theta = c\left(\mathbf{F}(\gamma_\theta) - \frac{\mathbf{F}(\gamma_\theta)\cdot \boldsymbol{w}_\theta}{\|\mathbf{F}(\gamma_\theta)\|}\,\boldsymbol{w}_\theta\right),$$

where $c > 0$ is such that $\|\boldsymbol{w}^{\boldsymbol{\Phi}}_\theta\| = 1$. The third and only additional basis vector in $\mathbb{R}^3$ is then simply the orthonormal vector to E^s_θ given by

$$\boldsymbol{w}^{\mathbf{n}}_\theta = \boldsymbol{w}_\theta \times \boldsymbol{w}^{\boldsymbol{\Phi}}_\theta,$$

yielding the orthonormal and right-handed coordinate system $(\boldsymbol{w}_\theta, \boldsymbol{w}^{\boldsymbol{\Phi}}_\theta, \boldsymbol{w}^{\mathbf{n}}_\theta)$ at γ_θ. Note that in $\mathbb{R}^n$ with $n > 3$, the required $n-2$ orthonormal vectors $\boldsymbol{w}^{\mathbf{n}_j}_\theta$ to E^s_θ can be constructed one-by-one via Gram–Schmidt orthonormalisation.

Figure 1 illustrates how the coordinate system $(\boldsymbol{w}_\theta, \boldsymbol{w}^{\boldsymbol{\Phi}}_\theta, \boldsymbol{w}^{\mathbf{n}}_\theta)$ is used to construct the fundamental segment $\boldsymbol{s}_\theta$ for the computation of the isochron $I_\theta(\Gamma^\times)$ on the stable manifold $W^s(\Gamma^\times)$ of $\Gamma^\times$. Panel (a) shows the saddle-type periodic orbit $\Gamma^\times$ with the constructed coordinate system based at γ_θ. Note that $\boldsymbol{w}_\theta$ and $\boldsymbol{w}^{\boldsymbol{\Phi}}_\theta$ span the plane E^s_θ, which also contains $\mathbf{F}(\gamma_\theta)$ and its the projections onto $\boldsymbol{w}_\theta$ and $\boldsymbol{w}^{\boldsymbol{\Phi}}_\theta$. The vector $\boldsymbol{w}^{\mathbf{n}}_\theta$ is the vector normal to E^s_θ.

To construct the fundamental segment we consider the one-parameter family of orbit segments $\boldsymbol{u}$ with integration time $T_{\Gamma^\times}$ whose end point lies along the stable Floquet direction from γ_θ, which is formalised by the boundary condition

$$\boldsymbol{u}_\eta(T_{\Gamma^\times}) = \gamma_\theta + \eta\,\boldsymbol{w}_\theta$$

with parameter $\eta \in \mathbb{R}^+$. Note that the orbit segment $\boldsymbol{\gamma}$ representing $\Gamma^\times$ is the solution of the BVP for $\eta = 0$. Hence, we find $\boldsymbol{u}_\eta$ by continuation in $\eta > 0$ from $\boldsymbol{u}_0 = \boldsymbol{\gamma}$. As η increases, the begin point $\boldsymbol{u}_\eta(0)$ moves away from γ_θ, as well as away from $\boldsymbol{w}_\theta$ and the latter is measured by the distance δ. The continuation is stopped when δ reaches a prescribed value $\delta_{\max}$ for some $\eta_{\delta_{\max}}$. Since $I_\theta(\Gamma^\times)$ is tangent to $\boldsymbol{w}_\theta$, we have that $\delta_{\max} = \eta^2_{\delta_{\max}}$. Moreover, for suffiently small $\eta_{\delta_{\max}}$, the begin point $\boldsymbol{u}_{\max}(0)$ of the final orbit $\boldsymbol{u}_{\max} = \boldsymbol{u}_{\eta_{\delta_{\max}}}$ lies (to good approximation) on $I_\theta(\Gamma^\times)$ and, thus, on the stable manifold $W^s(\Gamma^\times)$. Therefore, the two linear segments connecting the three points γ_0, $\boldsymbol{u}_{\max}(T_{\Gamma^\times})$ and $\boldsymbol{u}_{\max}(0)$ constitute a good approximation of a first and tiny piece of the isochron $I_\theta(\Gamma^\times)$, provided $\delta_{\max}$ is sufficiently small. In the examples of stable manifolds in Sections 3 and 4, $\delta_{\max}$ was set to 5×10^{-4}, and for the nonorientable manifold in Section 5 we used $\delta_{\max} = 5 \times 10^{-6}$.

The oriented line segment between $\boldsymbol{u}_{\max}(T_{\Gamma^\times})$ and $\boldsymbol{u}_{\max}(0)$, shown in Figure 1(b), is then sought fundamental segment $\boldsymbol{s}_\theta$; this choice is a direct generalisation to $\mathbb{R}^3$ of the construction of the fundamental segment for the planar case in [14]. Observe that the distance $\delta_{\max}$ of $\boldsymbol{u}_{\max}(0)$ to $\boldsymbol{w}_\theta$ is composed of the projected distances $\delta^{\boldsymbol{\Phi}}$ in E^s_θ and $\delta^{\mathbf{n}}$ normal to E^s_θ. We refer to the components $\delta^{\boldsymbol{\Phi}}$ and $\delta^{\mathbf{n}}$ as the *phase shear* and the *lift-off* of the isochron $I_\theta(\Gamma^\times)$, respectively. Note that $\delta^{\mathbf{n}} \neq 0$ when $W^s(\Gamma^\times)$ is nonlinear, which is the typical situation in practice. We find that the phase shear $\delta^{\boldsymbol{\Phi}}$ remains relatively small in all of our examples; this means, in practice, that $\delta_{\max} \approx \delta^{\mathbf{n}}$ primarily controls the lift-off from E^s_θ.

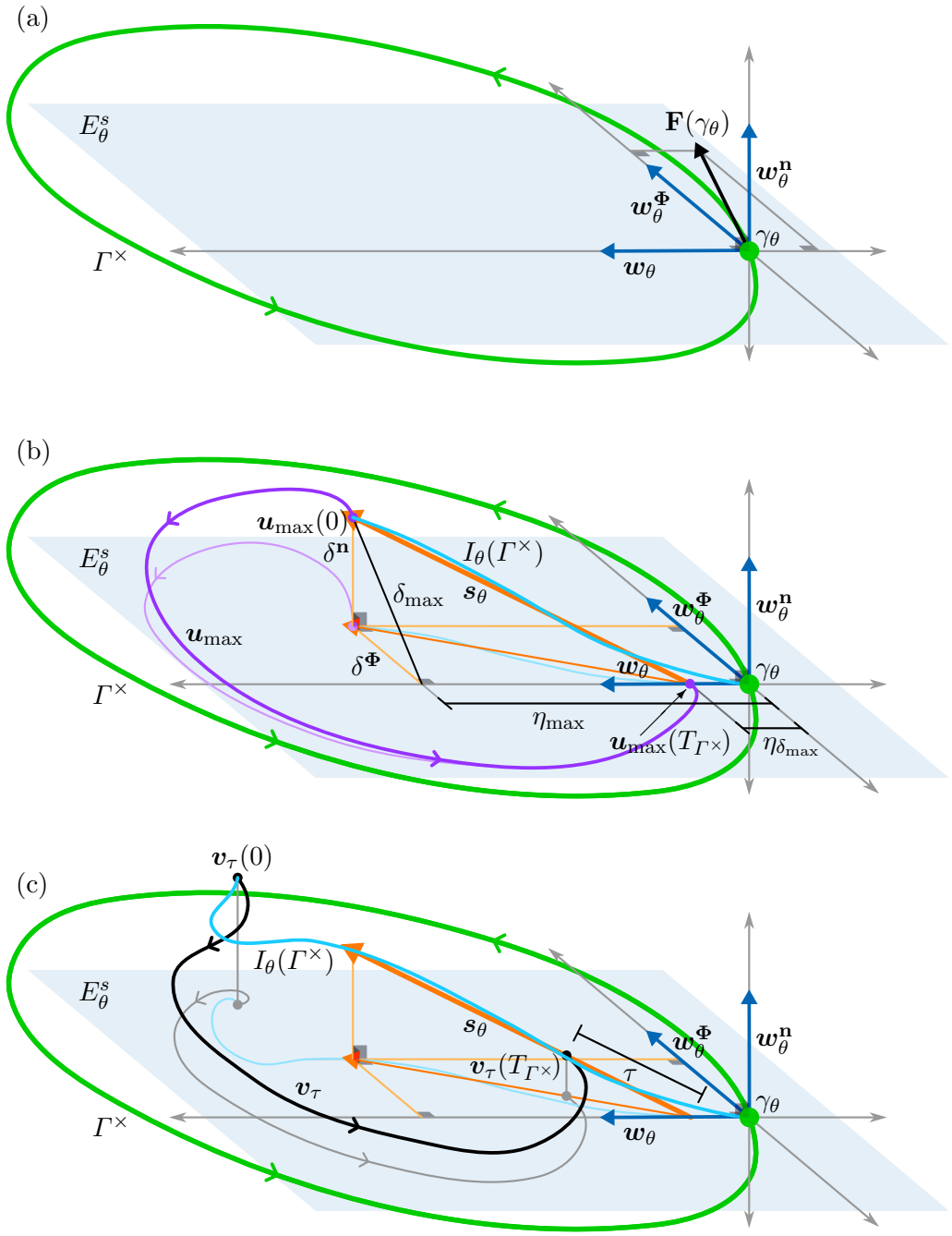

Figure 1: Set-up to compute the isochron $I_\theta(\Gamma^\times)$ (light-blue) at $\gamma_\theta \in \Gamma^\times$ on the two-dimensional stable manifold of a saddle-type periodic orbit $\Gamma^\times$ (green) in $\mathbb{R}^3$. Panel (a) shows the orthonormal basis $(\boldsymbol{w}_\theta, \boldsymbol{w}^{\mathbf{\Phi}}_\theta, \boldsymbol{w}^{\mathbf{n}}_\theta)$ (dark-blue) at γ_θ with $\mathbf{F}(\gamma_\theta)$. Panel (b) illustrates the construction of the fundamental segment $\boldsymbol{s}_\theta$ (orange), and panel (c) the orbit segment $\boldsymbol{x}_\tau$ used to grow $I_\theta(\Gamma^\times)$ by continuation in $\tau \in [0, 1]$.

2.2 Continuation of the isochron as a curve

The isochron algorithm now proceeds, as for the planar case [14, 23], by considering the one-parameter family of orbit segment $\boldsymbol{v}_\tau$ with integration time $T_{\Gamma^\times}$ and end point on the funda-

mental segment $\boldsymbol{s}_\theta = \boldsymbol{u}_{\max}(0) - \boldsymbol{u}_{\max}(T_{\Gamma^\times})$, which is defined by the boundary condition

$$\boldsymbol{v}_\tau(T_{\Gamma^\times}) = \gamma_\theta + \eta_{\delta_{\max}} \boldsymbol{w}_\theta + \tau \, \frac{\boldsymbol{u}_{\max}(0) - \boldsymbol{u}_{\max}(T_{\Gamma^\times})}{\|\boldsymbol{u}_{\max}(0) - \boldsymbol{u}_{\max}(T_{\Gamma^\times})\|} \,,$$

where $\tau \in [0,1]$. Note that $\boldsymbol{u}_{\max}$ satisfies this boundary condition, and with $\boldsymbol{v}_0 = \boldsymbol{u}_{\max}$ we perform a continuation in the family parameter τ. As Figure 1(c) illustrates, the begin point $\boldsymbol{v}_\tau(0)$ then traces out the isochron $I_\theta(\Gamma^\times) \subset W^s(\Gamma^\times)$. When $\tau = 1$ is reached, which means that $\boldsymbol{v}_1(T_{\Gamma^\times})$ has maximal distance $\delta_{\max}$, the algorithm switches to the continuation of an orbit segment with integration time $2T_{\Gamma^\times}$. The required extended orbit segment is obtained by appending to $\boldsymbol{v}_1$ the orbit segment $\boldsymbol{v}_0 = \boldsymbol{u}_{\max}$ that defines the fundamental segment $\boldsymbol{s}_\theta$; note that $\boldsymbol{v}_1(T_{\Gamma^\times}) = \boldsymbol{v}_0(0)$ by construction. This extended orbit segment is again continued in τ until $\tau = 1$ when the orbit segment is extended in the same way to one with integration time $3T_{\Gamma^\times}$, and so on until $I_\theta(\Gamma^\times)$ is obtained up to a chosen maximal arclength L. Note that $I_\theta(\Gamma^\times)$ is represented as an arlength-parametrised curve by a sequence of mesh points; the density of mesh points depends on the size of the continuation steps taken, which is determined by prescribed accuracy settings of the continuation.

Figure 1 illustrates the situation for an orientable manifold, but in $\mathbb{R}^n$ with $n \geq 3$, the manifold $W^s(\Gamma^\times)$ may be nonorientable; we will see an example of this in Section 5. In this case, the begin and end points of the orbit segments $\boldsymbol{u}_\eta$ for $\eta > 0$ are on either side of the plane spanned by $\boldsymbol{w}_\theta^{\boldsymbol{\Phi}}$ and $\boldsymbol{w}_\theta^{\mathbf{n}}$; in particular, the line segment between $\boldsymbol{u}_{\max}(0)$ and $\boldsymbol{u}_{\max}(T_{\Gamma^\times})$ does not define a fundamental segment. This issue is overcome by considering (multiples of) the second return time $2T_{\Gamma^\times}$ — defining the double-cover of the time-$T_{\Gamma^\times}$ map — in the construction of the fundamental segment $\boldsymbol{s}_\theta$.

Finally, we mention that the computational set-up for isochrons of foci in planar systems, as presented in [14, 23], can be generalised in the same way to compute (isochron foliations on) two-dimensional stable or unstable manifolds of saddle-foci in $\mathbb{R}^n$.

2.3 Representing and visualising the manifold

Obtaining a representation of $W^s(\Gamma^\times)$ requires the computation of isochrons $I_{\theta_i}(\Gamma^\times) \subset \mathcal{I}(\Gamma^\times)$ for a suitable finite subset $\theta_i \in [0,1]$; here we assume that all $I_{\theta_i}(\Gamma^\times)$ are computed up to the same maximal arclength L. In all our examples, we consider N_θ phase-uniform isochrons, meaning that $\theta_i = i/N_\theta$ for $i = 0, 1, \ldots (N_\theta - 1)$ for a suitable $N_\theta \in \mathbb{N}$. We remark that the orbit segment $\boldsymbol{\gamma}$ with $\boldsymbol{\gamma}(0) = \gamma_\theta$ and the associated Floquet bundle defining $\boldsymbol{w}_\theta$ can be rotated via continuation in the phase θ to obtain the required input for these K separate isochron computations; see [14, 24] for details.

The computed isochrons on the two-dimensional stable (or unstable) manifold can be used to render and visualise the respective manifold as a surface in different ways. Indeed, the foliation of the two-dimensional manifold of an oscillator by isochrons introduces a natural two-dimensional parametrisation that defines the point $\boldsymbol{x}(\theta, \ell)$ in terms of its asymptotic phase θ and arclength ℓ from the base point γ_θ along the isochron. It is straightforward to render the computed isochrons with base points γ_θ in $\mathbb{R}^3$ as a fan or comb of curves parametrised by $0 < \ell \leq L$. This already gives an impression of the two-dimensional manifold as a surface, as well as the phase dynamics on it. However, it is less straightforward (yet highly desirable) to visualise the manifolds directly as surfaces. This requires the construction of a suitable mesh, that is, a triangulation that can be rendered for visualisation; we use MATLAB for this purpose.

Depending on the geometry of the manifold and of the isochrons on it, generating a mesh of good quality may be a challenge. In light of the parametrisation property, a natural approach is to use a uniform mesh in (θ, ℓ)-space, that is, a triangulation generated from the points $\boldsymbol{x}(\theta_i, \ell_j)$ on the computed isochrons $I_{\theta_i}(\Gamma^\times)$. Here $0 \leq j \leq N_\ell$ for a chosen number N_ℓ of mesh

points on each of the N_θ isochrons. We assume further that these mesh points are distributed uniformly in arclength along each $I_{\theta_i}(\Gamma^\times)$, that is, $\ell_j = j/L$; note that this is readily achieved by interpolation of the computed points on each $I_{\theta_i}(\Gamma^\times)$ that are generated by the isochron manifold algorithm. Generating a triangulation from this phase- and arclength-uniform mesh to represent the surface $W^s(\Gamma^\times)$ works well near the periodic orbit $\Gamma^\times$ when the vectors $\boldsymbol{w}_{\theta_i}$ of its linear bundle are far from colinear with the tangent vector $\mathbf{F}(\gamma_{\theta_i})$; that is, the angle between $\boldsymbol{w}_{\theta_i}$ and $\mathbf{F}(\gamma_{\theta_i})$ is (reasonably) close to $\frac{\pi}{2}$. However, as we will see with the examples later in the section, already in this quite ideal local situation, this type of mesh may be less suitable further away from $\Gamma^\times$ because of nonlinear effects; specifically, a very uneven distance may arise between neighbouring computed isochrons as a function of their phase. The issue is that line segments between point $\boldsymbol{x}(\theta_i, \ell_j)$ and $\boldsymbol{x}(\theta_{i+1}, \ell_j)$ may become very large, which leads to very obtuse (narrow) triangles and, hence, a deterioration of the mesh quality.

To avoid the issue of obtuse triangles, we consider separate triangulations for the respective strips between each pair of successive isochrons, which we also refer to as phase ribbons. More optimal triangulations for such triangle strips are investigated in [35] and also in [25] in the context of triangulated ruled-surfaces, where triangulated strips arise from piecewise-linear interpolation between two discrete curves on a surface under consideration. Specifically, we attempt to connect a point $\boldsymbol{x}(\theta_i, \ell_j)$ on $I_{\theta_i}(\Gamma^\times)$ to the closest point on $I_{\theta_{i+1}}(\Gamma^\times)$, which we denote by $\boldsymbol{x}(\theta_{i+1}, \tilde{\ell}(j))$. For each j, the corresponding point at arclength $\tilde{\ell}(j)$ is determined by a search on the parametrised computed curve $I_{\theta_{i+1}}(\Gamma^\times)$. The triangulation of the respective phase ribbon is then generated from the resulting mesh points, and the surface rendered as the union of these ribbons.

We may take advantage of the representation of $W^s(\Gamma^\times)$ (or $W^u(\Gamma^\times)$) as the union of phase ribbons to illustrate and interpret the geometry of isochrons, whilst also highlighting the geometry of the manifold. This can be done in different ways, and in the examples later in this chapter we employ two types of visualisation. Firstly, it is informative to colour these phase ribbons according to a palette that depends on the phase θ; specifically, we use shades of blue for stable manifolds and shades or red for unstable manifolds. Secondly, we represent successive ribbons on the manifold alternatingly transparent and coloured by θ; the contrast between successive phase ribbons, in combination with a 'see-through' effect due to this transparency, provides additional insights into the interplay between the geometry of the manifold and the isochron foliation on it.

3 A constructed test-case example

In the spirit of planar models proposed by Winfree [38], we present the vector field

$$\begin{cases} \dot{x} = \beta x - (1-\kappa z)\,\omega y + \sigma x \dfrac{x^2+y^2}{1-\zeta z}, \\ \dot{y} = (1-\kappa z)\,\omega x + \beta y + \sigma y \dfrac{x^2+y^2}{1-\zeta z}, \\ \dot{z} = \alpha z, \end{cases} \tag{16}$$

which can be written in cylindrical-polar coordinates with $x + iy = re^{2\pi i\psi}$ as

$$\begin{cases} \dot{r} = \left(\beta + \sigma \dfrac{r^2}{1-\zeta z}\right) r, \\ \dot{\psi} = (1-\kappa z)\omega, \\ \dot{z} = \alpha z, \end{cases} \tag{17}$$

For any values of the parameters, system (16) is invariant under rotation about the z-axis, as can be seen from the fact that the equations for $\dot{r}$ and $\dot{z}$ of system (17) are decoupled from that for $\dot{\psi}$. Moreover, the (x, y)-plane is always invariant and the dynamics on it is given by the first two equations of (16) and (17) with $z = 0$, which is the (planar) normal-form of the Hopf bifurcation [11, 21, 32].

We are interested in the supercritical case with $\sigma < 0$, and also take $\alpha > 0$ so that the z-direction is expanding. Then for $\beta > 0$, and any value of ζ and κ, the system has a saddle periodic orbit $\Gamma^\times$ in the (x, y)-plane, which has radius $\sqrt{|\beta/\sigma|}$ and frequency ω. Due to invariance, the (x, y)-plane is the stable manifolds $W^s(\Gamma^\times)$, with the exception of the origin (which is a repelling equilibrium); note that the frequency of rotation on $W^s(\Gamma^\times)$ is ω irrespective of the radius r since here $z = 0$. Hence, each forward-time isochron $I_\theta(\Gamma^\times) \subset W^s(\Gamma^\times)$ is the straight ray from the origin in the (x, y)-plane through the point $\gamma_\theta \in \Gamma^\times$. Due to the rotational invariance, the unstable manifold $W^u(\Gamma^\times)$ is a surface of revolution, and the isochrons of both $\mathcal{I}(\Gamma^\times)$ and $\mathcal{U}(\Gamma^\times)$ map to one another, respectively, under any rotation about the z-axis.

3.1 The standard saddle periodic orbit

We first consider the case $\zeta = 0$, when the equation for $\dot{r}$ in (17) is decoupled from those for $\dot{\psi}$ and $\dot{z}$. Therefore, the unstable manifold of $\Gamma^\times$ is the orthogonal, straight cylinder

$$W^u(\Gamma^\times) = \{(x, y, z) \in \mathbb{R}^3 \,|\, x^2 + y^2 = -\frac{\beta}{\sigma}\},$$

and we refer to $\Gamma^\times$ as the *standard saddle periodic orbit*. The parameter κ determines how the frequency of rotation, which is constant in planes $z = const$ and given by the angular velocity $\dot{\psi}$, deviates from ω as a function of z. For $\kappa = 0$, we have that $\dot{\psi} = \omega$ for any z, so that the time-$T_{\Gamma^\times}$ map preserves any plane with $\theta = const$. As a result, each isochron $U_\theta(\Gamma^\times) \subset W^u(\Gamma^\times)$ is a vertical straight line through the point $\gamma_\theta \in \Gamma^\times$. For $\kappa \neq 0$, on the other hand, the angular velocity about the z-axis, as given by the equation for $\dot{\psi}$ in (17), changes linearly with z. For $\kappa > 0$, the effective angular velocity is larger for $z < 0$ and smaller for $z > 0$; thus, trajectories on $W^u(\Gamma^\times)$ lag behind $\Gamma^\times$ above the (x, y)-plane, while below it, they move increasingly faster than $\Gamma^\times$ in terms of the polar angle ψ. As a result of this linear decrease/increase of the angular velocity with z, the backward-time isochrons $U_\theta(\Gamma^\times) \in \mathcal{U}(\Gamma^\times)$ are no longer straight lines but spirals — specifically, they are helices with slope $\frac{\omega}{\kappa}$ at $\Gamma^\times$ — that together form the straight cylinder $W^s(\Gamma^\times)$.

We now employ the isochron computation algorithm for saddle periodic orbits in $\mathbb{R}^3$ to compute the global invariant manifolds of the standard saddle periodic orbit $\Gamma^\times$. In our computations, we fix $\beta = 4$, $\sigma = -1$, $\omega = 2$, and $\alpha = 1$ throughout, so that $\Gamma^\times$ has radius 2. Specifically, we compute and show 25 forward-time isochrons on $W^s(\Gamma^\times)$ and 25 backward-time isochrons on $W^u(\Gamma^\times)$, each up to maximal arclength $L = 10$ and uniformly distributed in phase; the number of isochrons is kept quite low here purely for illustration purposes. The results for $\kappa = 0$ and for $\kappa = 0.5$ are shown in (x, y, z)-space in Figure 2.

Row (a) of Figure 2 for $\kappa = 0$ shows that, the computed isochrons are as expected: the forward-time isochrons $I_\theta(\Gamma^\times) \subset W^s(\Gamma^\times)$ are straight rays in the (x, y)-plane, and the backward-time isochrons $U_\theta(\Gamma^\times) \subset W^u(\Gamma^\times)$ are vertical straight lines. Panel (a1) shows $W^s(\Gamma^\times)$ and $W^u(\Gamma^\times)$ as surfaces rendered from the respective 25 computed isochrons, where colour is used to indicate the associated phase on the two manifolds. Panel (a2) illustrates the geometry of, and the phase information on $W^s(\Gamma^\times)$ and $W^u(\Gamma^\times)$ by showing alternatingly coloured and transparent phase ribbons, each of which has a phase width of $\Delta\theta = \frac{1}{25}$. This highlights the computed isochrons as curves along which the colour changes and, moreover, creates a 'see-through' effect that enhances the three-dimensional nature of the image. This type of illustration

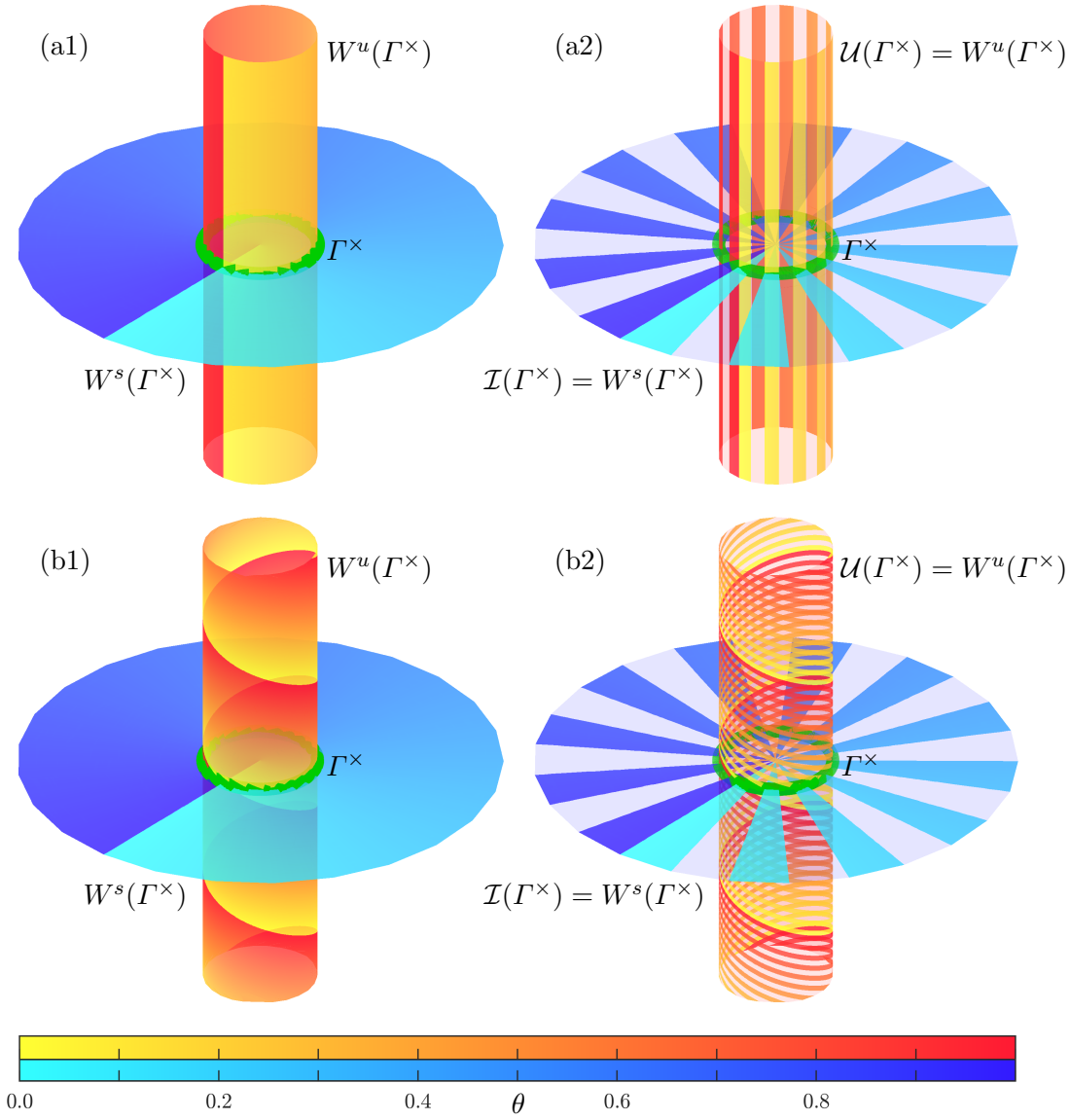

Figure 2: Computed isochrons on the global invariant manifolds of the standard periodic orbit $\Gamma^\times$ (green curve) of system (16) with $\zeta = 0$, for $\kappa = 0$ in row (a) and for $\kappa = 0.5$ in row (b). The left column shows the manifolds $W^s(\Gamma^\times)$ (cyan–blue surface) and $W^u(\Gamma^\times)$ (yellow–red surface) up to maximal arclength $L = 10$ and coloured according to their phase θ as given by the colour bars. The right column shows the same manifolds divided into alternatingly coloured and transparent phase ribbons of phase width $\Delta\theta = \frac{1}{25}$. The same phase colouring is used in all subsequent figures.

also highlights where isochrons are closer to or further away from each other in Euclidean distance in phase space, which indicates slower or faster dynamics along trajectories in the respective regions on the invariant manifold.

Row (b) of Figure 2 shows, in the same way, the computed isochrons for $\kappa = 0.5$. As predicted, the forward-time isochrons $I_\theta(\Gamma^\times) \subset W^s(\Gamma^\times)$ are unchanged, but the backward-time isochrons $U_\theta(\Gamma^\times)$ are now spirals on the straight cylinder $W^u(\Gamma^\times)$; this is especially visible in the representation by phase ribbons in panel (b2). We stress that the manifold $W^u(\Gamma^\times)$ has now been rendered as the union of 25 spiralling phase ribbons bounded by neighbouring computed isochrons. Comparison of the rendered surfaces $W^u(\Gamma^\times)$ in row (b) with those in

row (a) illustrates that this manifold is computed and rendered accurately as the cylinder of radius 2, in spite of the spiralling nature of the isochrons on it.

3.2 The funnel saddle periodic orbit

For $\zeta \neq 0$, the unstable manifold $W^u(\Gamma^\times)$ is no longer given explicitly and needs to be found numerically. For small ζ and locally near $\Gamma^\times$, this invariant manifold is a perturbation of the cylinder for $\zeta = 0$. However, its global properties are quite different. Notice from the equation for $\dot{r}$ of (17) that the flow in the r-direction blows up for $z \to \frac{1}{\zeta}$, while it remains bounded in the z-direction. This means that the manifold $W^u(\Gamma^\times)$ approaches the plane with $z = \frac{1}{\zeta}$. For $z \to \pm\infty$, on the other hand, $\dot{r}$ is bounded, while $\dot{z} \to \pm\infty$; hence $W^u(\Gamma^\times)$ becomes practically vertical for large $|z|$. These asymptotic properties mean that $W^u(\Gamma^\times)$ has the shape of a funnel, and we refer to $\Gamma^\times$ when $\zeta \neq 0$ as a *funnel saddle periodic orbit*. As we found for the standard periodic orbit in Section 3.1, when $\kappa = 0$, the isochron $U_\theta(\Gamma^\times)$ is the intersection of the funnel with the half-plane of angle $\psi = \theta$ with respect to the positive real axis. For $\kappa \neq 0$, on the other hand, the isochrons in $\mathcal{U}(\Gamma^\times)$ spiral around this same funnel.

Figure 3 shows the surfaces $W^s(\Gamma^\times)$ and $W^u(\Gamma^\times)$ in (x, y, z)-space of the funnel saddle periodic orbit $\Gamma^\times$ of system (16) with $\zeta = -\frac{1}{11}$, as computed with the isochron computation algorithm, for $\kappa = 0$ in row (a) and for $\kappa = 0.5$ in row (b). As before, these surfaces have been rendered from 25 phase-uniform isochrons each, and they are shown in the region of interest given by $r = \sqrt{x^2 + y^2} \leq 15$ and $-11 \leq z \leq 8$. The style of presentation is as in Figure 2 with panels (a1) and (b1) showing the phase on $W^s(\Gamma^\times)$ and $W^u(\Gamma^\times)$ with a continuous colour, while panels (a2) and (b2) show alternatingly coloured and transparent phase ribbons. Notice in Figure 3 that, as expected, the stable manifold $W^s(\Gamma^\times)$ is unaffected by the fact that $\zeta \neq 0$. The unstable manifold $W^u(\Gamma^\times)$, on the other hand, is no longer a straight cylinder, but has the predicted characteristic funnel shape: it approaches the asymptotic plane defined by $z = \frac{1}{\zeta} = -11$ and does not exist for $z \leq -11$. In row (a) of Figure 3, for $\kappa = 0$, the backward-time isochrons $U_\theta(\Gamma^\times) \subset W^u(\Gamma^\times)$ are curves with fixed polar angle ψ for any $z > -11$, as is illustrated nicely by the phase ribbons in panel (a2). In row (b) for $\kappa = 0.5$, the geometry of the surface $W^u(\Gamma^\times)$ is the same, but the backward-time isochrons $U_\theta(\Gamma^\times) \subset W^u(\Gamma^\times)$ now spiral around the funnel $W^u(\Gamma^\times)$. Notice that the rotation is very pronounced where the funnel is quite narrow, but comes to a halt as the isochrons $U_\theta(\Gamma^\times) \subset W^u(\Gamma^\times)$ approach the asymptotic plane; see panel (b2). This observation is explained by the fact that $\dot{r}$ blows up as $z \to \frac{1}{\zeta} = -11$ (while $\dot{z}$ is bounded for $z = -11$).

Comparison of Figure 3 with Figure 2 shows that, locally near $\Gamma^\times$, the surface $W^u(\Gamma^\times)$ for $\zeta = -\frac{1}{11}$ is indeed a perturbation of the cylinder $W^u(\Gamma^\times)$ for $\zeta = 0$; moreover, for either value of κ, the isochrons $U_\theta(\Gamma^\times) \subset W^u(\Gamma^\times)$ for $\zeta = -\frac{1}{11}$ are close to those for $\zeta = 0$ near $\Gamma^\times$. As for the standard saddle periodic orbit, we find that $W^u(\Gamma^\times)$ is computed accurately also for $\zeta = -\frac{1}{11}$, irrespective of whether the isochrons spiral or not. Indeed, there are no discernible differences between the two computed manifolds $W^u(\Gamma^\times)$, for $\kappa = 0$ in row (a) and for $\kappa = 0.5$ in row (b) of Figure 3, when viewed as a surface; more precisely, the difference between the two triangulations is on the order of the interpolation error between mesh points. This demonstrates that the isochron manifold algorithm is capable of computing two-dimensional global manifolds of a saddle periodic orbit reliably and accurately. Moreover, it allows one to investigate the interplay between the geometry of these surfaces and the phase dynamics on them, as we will now illustrate with two more general examples without special symmetry properties.

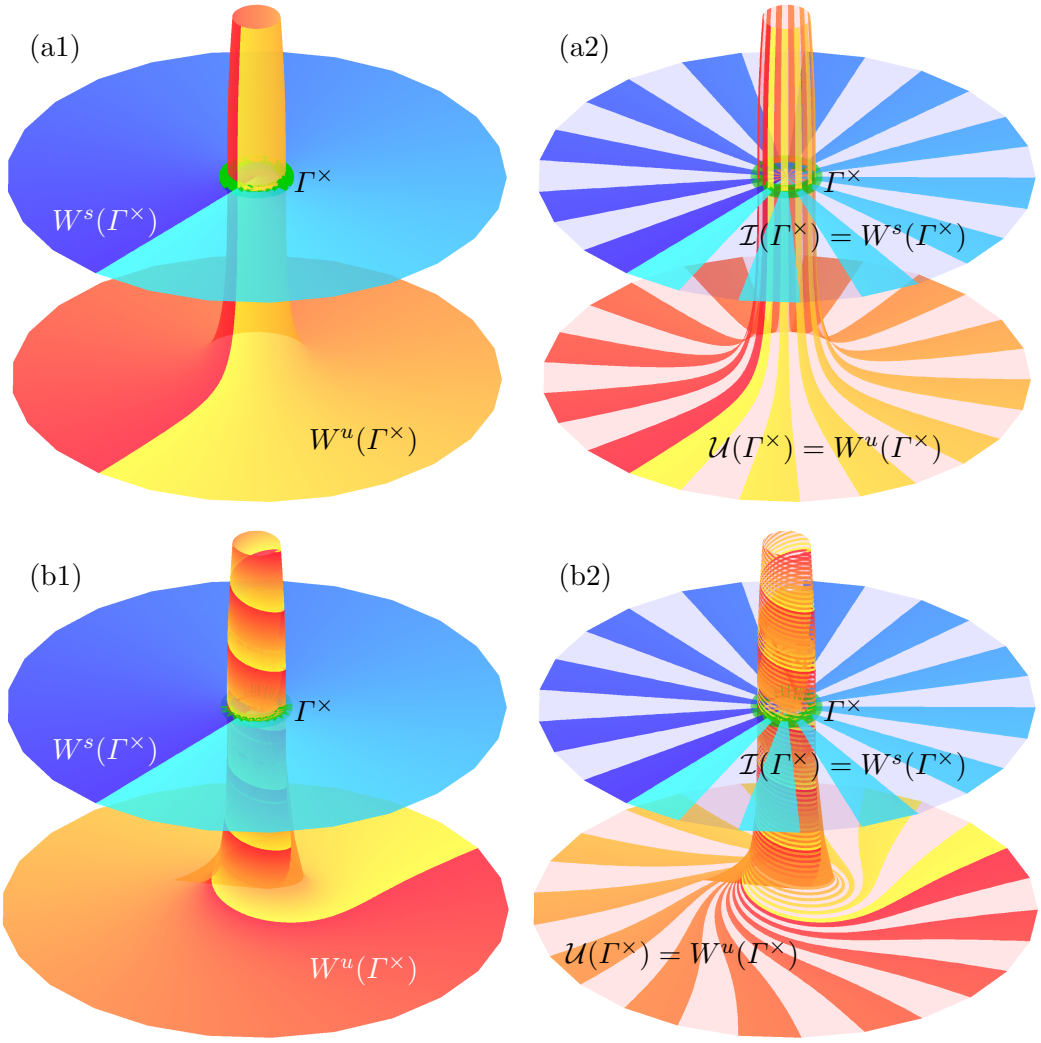

Figure 3: Computed isochrons on the global invariant manifolds of the funnel periodic orbit $\Gamma^\times$ (green curve) of system (16) with $\zeta = -\frac{1}{11}$, for $\kappa = 0$ in row (a) and for $\kappa = 0.5$ in row (b). Rendering and colours are as in Figure 2.

4 Orientable manifold in Sandstede's model

Sandstede [29] designed the model system, given as the three-dimensional vector field

$$\begin{cases} \dot{x} = ax + by - ax^2 + x(2-3x)(\tilde{\mu} - \alpha z), \\ \dot{y} = bx + ay - \dfrac{3}{2}(bx^2 + axy) - 2y(\tilde{\mu} - \alpha z), \\ \dot{z} = cz + \mu x + \gamma xz + \alpha\beta\left(x^2(1-x) - y^2\right), \end{cases} \tag{18}$$

to explore different types of homoclinic bifurcations; for example, see [1, 8, 9, 26] for numerical investigations of different global bifurcations in this system. We use (18) here as a convenient example of a three-dimensional system. Based on information from [8, 9], we fix the different parameter to $a = 0.22$, $b = 1.0$, $c = -2.0$, $\alpha = 0.3$, $\beta = 1.0$, $\gamma = 2.0$, $\mu = 0.004$, and $\tilde{\mu} = 0$, so that system (18) has a saddle periodic orbit $\Gamma^\times$ that is orientable; this means that $\Gamma^\times$ has positive Floquet multipliers so that $W^s(\Gamma^\times)$ and $W^u(\Gamma^\times)$ are topological cylinders/annuli near $\Gamma^\times$. The system is quite close to a homoclinic bifurcation of the origin $\mathbf{0}$ where $\Gamma^\times$ bifurcates (when $\mu = 0$), and the unstable manifold $W^u(\Gamma^\times)$ is bounded by the one-dimensional unstable

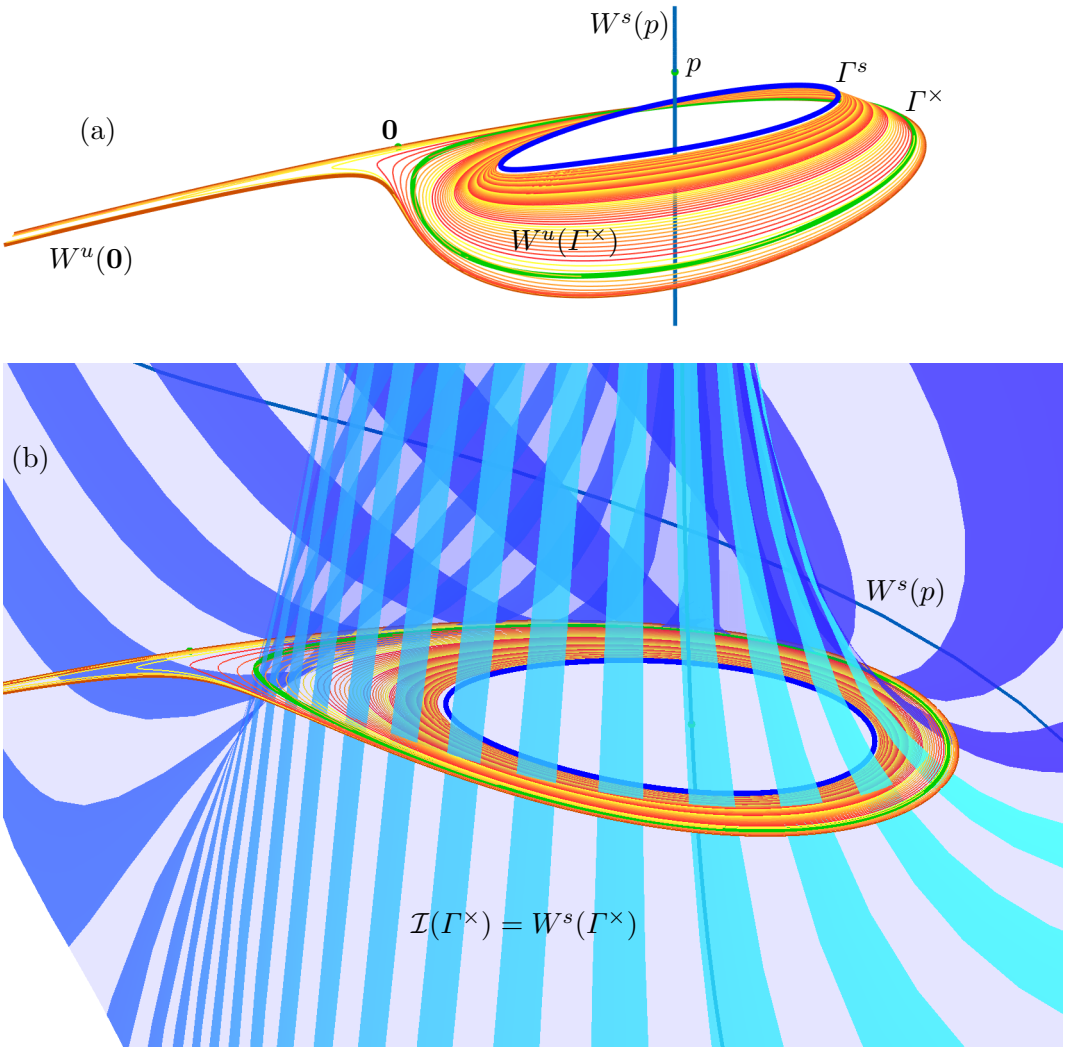

Figure 4: Phase portrait of system (18) near the saddle periodic orbit $\Gamma^\times$. Panel (a) shows $\Gamma^\times$ (green curve), the saddle points $\mathbf{0}$ (green dot) and p (green dot), their one-dimensional manifolds $W^u(\mathbf{0})$ (red curve) and $W^s(p)$ (blue curve), and the stable periodic orbit Γ^s (blue curve); also shown are 100 phase-uniform backward-time isochrons $U_\theta(\Gamma^\times) \subset W^u(\Gamma^\times)$ (yellow–red curves). Panel (b) is a slightly different view and also shows $W^s(\Gamma^\times)$ represented by 50 alternating phase ribbons.

manifold $W^u(\mathbf{0})$ on one side and by an attracting periodic orbit Γ^s on the other. Nearby is a second saddle equilibrium p with a one-dimensional stable manifold $W^s(p)$ that is 'surrounded' by Γ^s.

Figure 4 illustrates these invariant objects in (x, y, z)-space. Here, $\Gamma^\times$, $\mathbf{0}$, $W^u(\mathbf{0})$, Γ^s, p, and $W^s(p)$ are found with standard continuation techniques as implemented in the package AUTO [5], while the surfaces $W^s(\Gamma^\times)$ and $W^u(\Gamma^\times)$ are computed with the isochron manifold algorithm. Panel (a) does not show $W^s(\Gamma^\times)$ and focuses on the unstable manifold $W^u(\Gamma^\times)$, which is represented by 100 computed phase-uniform backward-time isochrons $U_{\theta_i}(\Gamma^\times) \subset W^u(\Gamma^\times)$. The computed isochrons are seen spiralling very tightly as they extend from $\Gamma^\times$ and accumulate onto the attracting periodic orbit Γ^s. On the other side of $\Gamma^\times$, the backward-time isochrons accumulate onto the curve $W^u(\mathbf{0})$, which has two branches that both tend to infinity along the same direction to the left of the image. In the process, the isochrons on $W^u(\mathbf{0})$ feature larger and larger excursions towards infinity as they keep spiralling around $\Gamma^\times$. Panel (b) shows

a slightly different view, where the stable manifold $W^s(\Gamma^\times)$ is now also shown. This surface was rendered from 200 computed phase-uniform forward-time isochrons $I_{\theta_i}(\Gamma^\times) \subset W^s(\Gamma^\times)$ of arclength $L = 5$; it is shown here as 50 alternating ribbons of equal phase width. Notice that p and the first part of the curve $W^s(p)$ are obscured by a coloured phase ribbon; however, the lower branch of $W^s(p)$ bends around and re-enters the image on the right of the image.

Figure 4 shows that the computed backward-time isochrons $U_{\theta_i}(\Gamma^\times)$ are extremely close to each other and already give a good impression of the geometry of the unstable manifold $W^u(\Gamma^\times)$, which has the shape of a tennis racket and lies very close to the (x, y)-plane of system (18). However, due to the closeness of the bounding curves Γ^s and $W^u(\mathbf{0})$ to the saddle-periodic orbit $\Gamma^\times$, in combination with the strongly spiralling nature of the backward-time isochrons, it is impractical to render $W^u(\mathbf{0})$ as a triangulated surface from this data. The stable manifold $W^s(\Gamma^\times)$, on the other hand, can be rendered effectively from the computed forward-time isochrons $I_{\theta_i}(\Gamma^\times)$. This surface is a cylinder, but panel (b) also hints at some interesting geometry and phase dynamics.

Figure 5 shows a more global view of the surface $W^s(\Gamma^\times)$ as rendered from the computed forward-time isochrons of arclength $L = 5$; for balance of the images, $W^s(\Gamma^\times)$ has been clipped here at the top, namely at $z = 3$. As in Section 3, we show $W^s(\Gamma^\times)$ in two ways: rendered with asymptotic phase shown in colour in panel (a), and as alternatingly coloured and transparent ribbons of phase width $\Delta\theta = \frac{1}{50}$ in panel (b). This larger view shows that $W^s(\Gamma^\times)$ has a distinctive funnel shape near $\Gamma^\times$, which is quite similar to that of the unstable manifold $W^u(\Gamma^\times)$ of system (16); compare with Figure 3. More specifically, the top part of $W^s(\Gamma^\times)$ narrows in Figure 5 and approaches the curve $W^s(p)$, while its lower part becomes very wide. Notice, however, that $W^s(\Gamma^\times)$ does not approach an invariant plane, as $W^u(\Gamma^\times)$ does in Figure 3, but rather starts to bend upward on the left of the image, towards the region of positive z.

While Figure 5(a) gives a very good impression of the geometry of $W^s(\Gamma^\times)$, the phase ribbon structure of Figure 5(b) allows us to point out some interesting aspects of the phase dynamics. First of all, locally near $\Gamma^\times$ the isochrons on $W^s(\Gamma^\times)$ are practically vertical (well aligned with the z-direction), as is the case for $W^u(\Gamma^\times)$ of system (16) with $\kappa = 0$; compare with Figure 3(a2). In contrast to the constructed example, however, the isochrons $I_\theta(\Gamma^\times) \subset W^s(\Gamma^\times)$ of system (18) cannot be mapped to one another by a fixed rotation. Moreover, the different widths of the phase ribbons in the lower part of $W^s(\Gamma^\times)$ in Figure 5(a) show that this manifold contains regions where the flow is faster as well as where it is slower relative to the mean speed of the dynamics on the manifold. Similarly, the spacing of phase ribbons in the upper part of $W^s(\Gamma^\times)$ becomes quite non-uniform as the surface approaches the curve $W^s(p)$.

Figures 6 and 7 show the invariant objects of system (18) in a much larger part of (x, y, z)-space. The manifold $W^s(\Gamma^\times)$ is shown as a smooth surface with asymptotic phase information in Figure 6, while Figure 7 shows it as represented by alternatingly coloured and transparent phase ribbons. Here, $W^s(\Gamma^\times)$ is rendered from the same 200 phase-uniform forward-time isochrons that have now been computed up to maximal arclength $L = 20$, without any clipping. The angle of view in panels (a) is very similar to that in Figure 5(b), and panels (b) is a view from 'the back'. Figures 6 and 7 illustrate that, further away from $\Gamma^\times$, the topological cylinder $W^s(\Gamma^\times)$ has quite an intriguing geometry with large changes of its local (Gaussian) curvature. Notice how the upper part of $W^s(\Gamma^\times)$ approaches $W^s(p)$ very closely as z increases, forming a 'spire', while the isochrons are rotating more and more around $W^s(p)$; this rotation accounts for the spire being quite short compared to the arclength $L = 20$ of the isochrons that form it. The lower part of $W^s(\Gamma^\times)$, on the other hand, grows quite a bit with arclength, as is illustrated by the wider spacing between the phase ribbons in Figure 7. Notice from Figure 6 that, nevertheless, the 200 computed isochrons still allow us to render $W^s(\Gamma^\times)$ as a surface with a triangulation of good quality.

From the far vantage points in Figure 7, we can see that the isochrons foliating $W^s(\Gamma^\times)$

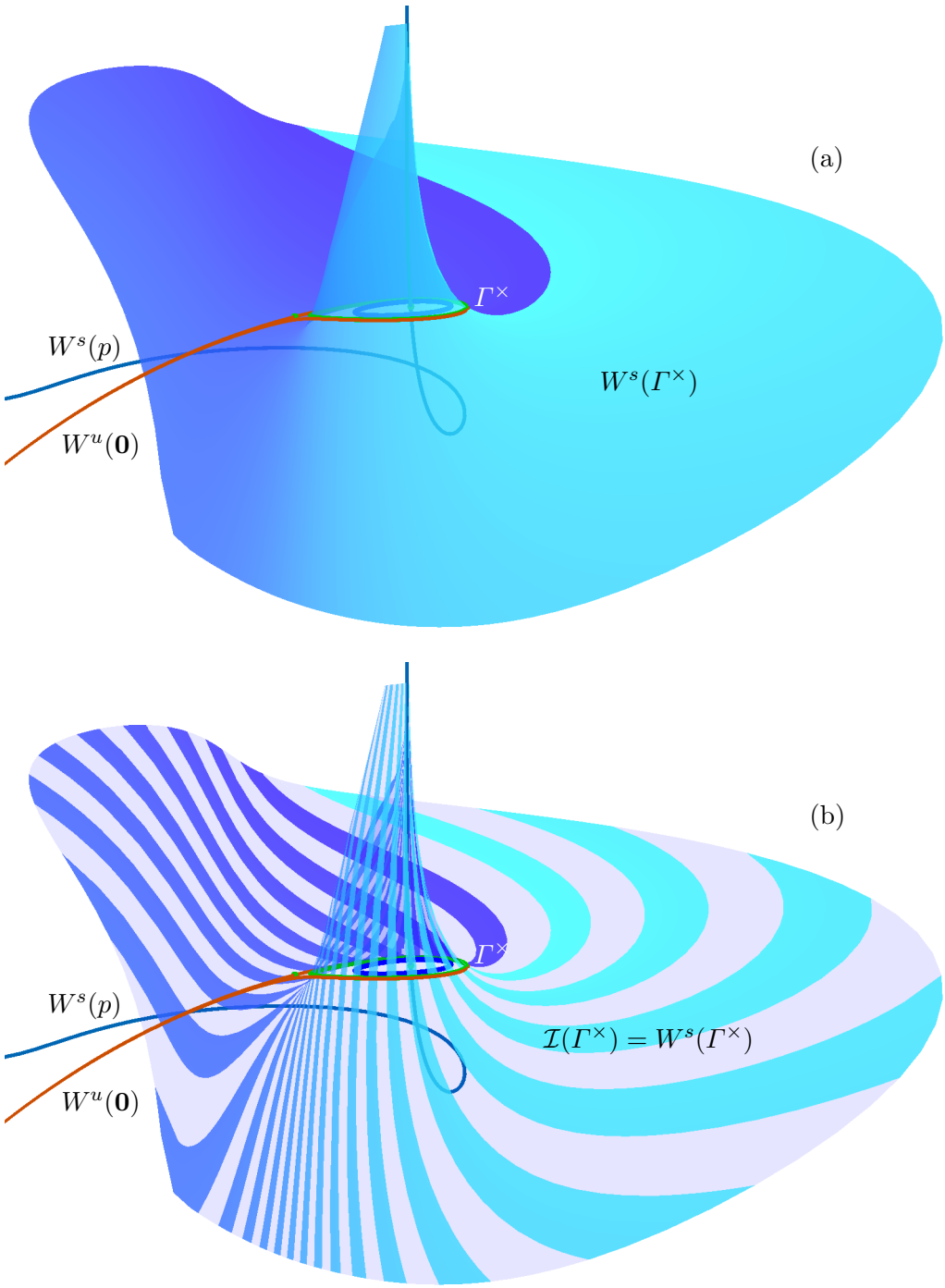

Figure 5: An expanded view of $W^s(\Gamma^\times)$ and the invariant objects from Figure 4. The manifold is rendered from 200 phase-uniform forward-time isochrons of arclength $L = 5$. This view is clipped at $z = 3$, and $W^s(\Gamma^\times)$ is shown phase-coloured in panel (a), and as 50 alternating phase ribbons in panel (b).

partially mimic the geometry of this surface by following its folding. There are regions where $\mathcal{I}(\Gamma^\times)$ is nearly orthogonal to the boundary of $W^s(\Gamma^\times)$ computed up to $L = 20$, as well as regions where $\mathcal{I}(\Gamma^\times)$ almost appearsto be tangent to this boundary. In fact, the isochrons are transverse to the boundary everywhere, but where the surface $W^s(\Gamma^\times)$ has high curvature the respective isochrons tend to have more acute angles with the boundary. This phenomenon can

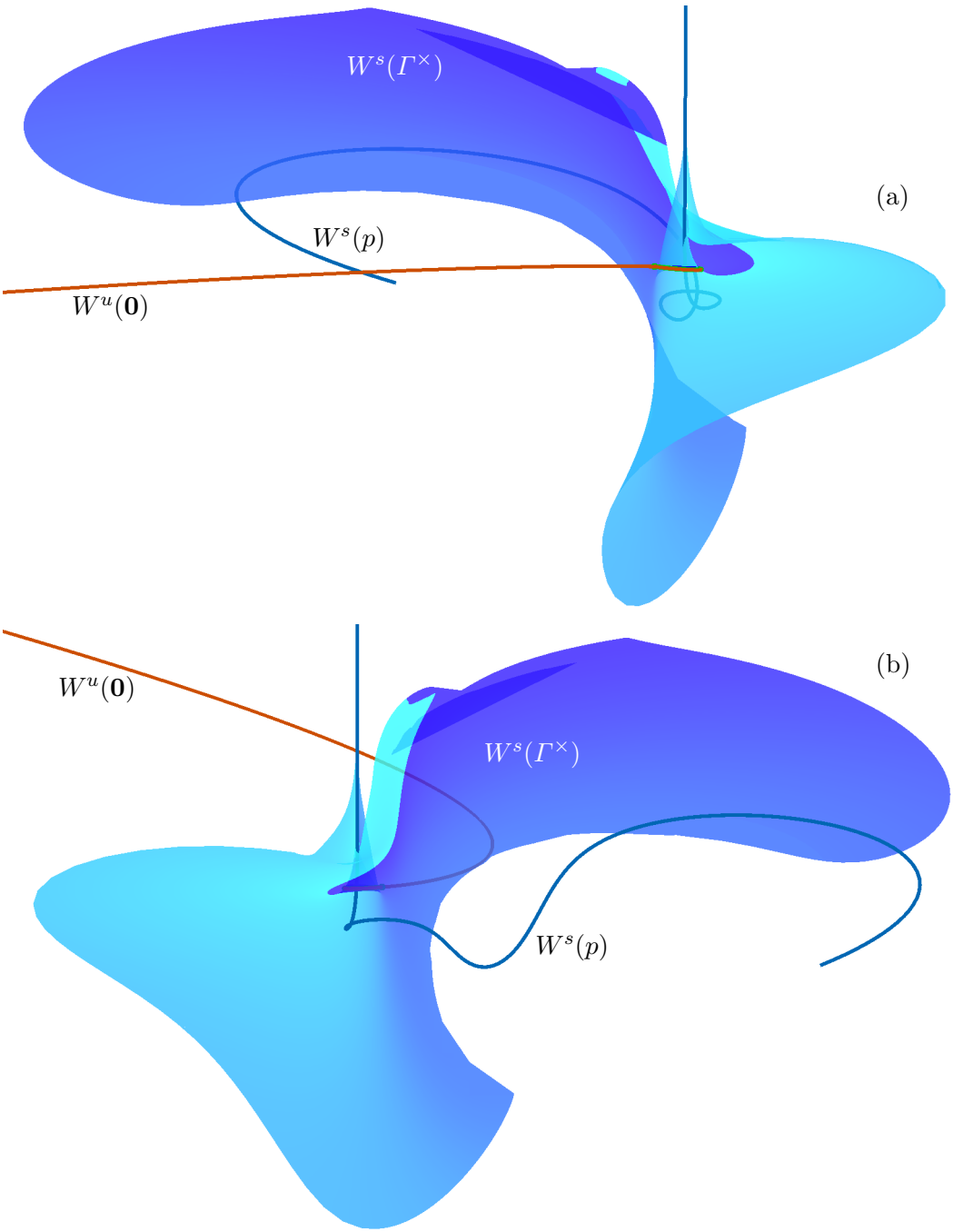

Figure 6: Two more global views of the invariant objects from Figure 5, where $W^s(\Gamma^\times)$ is rendered from 200 phase-uniform isochrons of arclength $L = 20$ and coloured by phase.

be observed in Figure 6(b) for phases near $\theta = 0$ on the lower portion of $W^s(\Gamma^\times)$. Here, $W^s(\Gamma^\times)$ has an extreme fold, along which the isochrons $I_\theta(\Gamma^\times)$ also fold sharply. The large width of the phase-ribbons here indicates relatively fast dynamics along this part of the manifold. We see a similar, though less extreme, example of this folding on the left-hand side of Figure 6(b). In contrast, clearly transverse intersection of $\mathcal{I}(\Gamma^\times)$ with the boundary of $W^s(\Gamma^\times)$ can be observed along the left and bottom sides of Figure 6(a) and along the bottom side of Figure 6(b), where $W^s(\Gamma^\times)$ has low curvature and relatively slower dynamics.

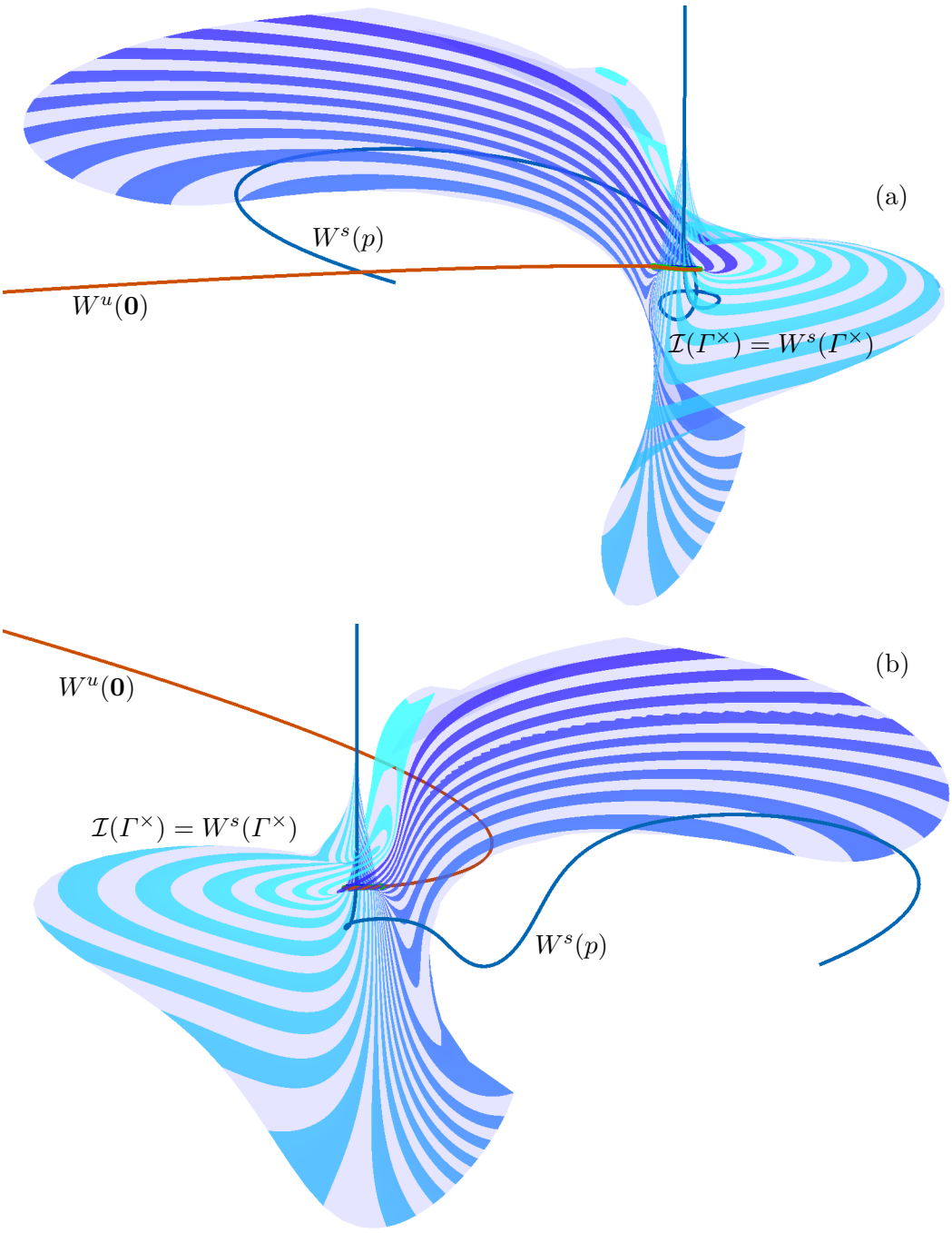

Figure 7: The same objects and views as in Figure 6, where $W^s(\Gamma^\times)$ is now shown as alternating phase ribbons.

5 Nonorientable manifold in the ζ^3-model

We now show that the isochron manifold algorithm is effective also when the saddle periodic orbit $\Gamma^\times$ has a pair of negative real Floquet multipliers, a stable one inside and an unstable one outside the unit circle. The stable and unstable manifolds $W^s(\Gamma^\times)$ and $W^u(\Gamma^\times)$ are then nonorientable, which means that they are Möbius bands locally near $\Gamma^\times$. Following previous work on the computation of nonorientable manifolds in [27], we choose to consider such a saddle

periodic orbit in the ζ^3-model

$$\begin{cases} \dot{x} = y, \\ \dot{y} = z, \\ \dot{z} = (\alpha - x)x - \beta y - z, \end{cases} \tag{19}$$

which was introduced by Arneodo *et al.* [3]. For $\alpha = 3.2$ and $\beta = 2.0$, the ζ^3-model (19) has a saddle equilibrium p with a one-dimensional stable manifold $W^s(p)$. This curve is surrounded (close to p) by a saddle periodic orbit $\Gamma^\times$ with negative Floquet multipliers as well as an attracting period-doubled orbit Γ^s. Moreover, the origin $\mathbf{0}$, which is always an equilibrium of system (19), is a saddle and one branch of its one-dimensional unstable manifold $W^u(\mathbf{0})$ accumulates onto Γ^s. All these invariant objects are readily found with AUTO [5]. The two-dimensional unstable manifold $W^u(\Gamma^\times)$ is a narrow Möbius band that is bounded by Γ^s; we do not show $W^u(\Gamma^\times)$ here, but see [27] for more details and images. Rather, we focus on the nonorientable and unbounded stable manifold $W^s(\Gamma^\times)$, which we render from 200 phase-uniform forward time isochrons computed with the isochron manifold algorithm.

The phase portrait of system (19) near the saddle periodic orbit $\Gamma^\times$ is shown in Figure 8. More specifically, all invariant objects mentioned above are shown with $W^s(\Gamma^\times)$ computed and visualised with forward-time isochrons of $\mathcal{I}(\Gamma^\times)$ of arclength $L = 8$. In panel (a), the computed local part of $W^s(\Gamma^\times)$ is rendered as a surface coloured by asymptotic phase, which shows that it is, indeed, a Möbius band. The rendering by phase ribbons, shown in panel (b), illustrates how the isochrons of $\mathcal{I}(\Gamma^\times)$, when continued along $\Gamma^\times$, fold over in the process to connect up with a half-twist — just as is the case when one makes a Möbius band (as a developable surface) from a thin strip of paper by giving it a half-twist along its length and glueing it along its short sides. Notice also that the isochrons are almost perpendicular to $\Gamma^\times$ and that the phase ribbons all have a very similar width. On the other hand, and in contrast to a twisted (flat) strip of paper, the isochrons and the Möbius band are curved quite a bit, especially in the bottom-right of the figure where they fold over quite suddenly.

Figure 9 shows $W^s(\Gamma^\times)$ from the same angle and position near $\Gamma^\times$, but now the manifold $W^s(\Gamma^\times)$ has been rendered from isochrons of $\mathcal{I}(\Gamma^\times)$ of arclength $L = 100$; to allow for a direct comparison with Figure 8, all global objects have been clipped to lie in the cube $[0, 5] \times [-4, 4] \times [-5, 4] \subset \mathbb{R}^3$. Figure 9 illustrates that the Möbius band $W^s(\Gamma^\times)$ approaches the stable manifold $W^s(p)$ in a spiralling fashion near the point p. In the process, the isochrons of $\mathcal{I}(\Gamma^\times)$ perform a half-twist with every rotation around $\Gamma^\times$. Note that the local curvature where the isochrons fold over becomes larger and larger, which is particularly visible in Figure 9(b) where $W^s(p)$ is rendered by alternating phase ribbons.

Figures 10 and 11 show the invariant objects of system (19) in a much larger part of (x, y, z)-space to give a complete impression of the entire Möbius band $W^s(\Gamma^\times)$ as rendered from 200 phase-uniform isochrons of arclength $L = 100$. Each figure shows the invariant objects from the same two view points, with $W^s(\Gamma^\times)$ rendered as a smooth phase-coloured surface in Figure 10 and as alternating phase ribbons in Figure 11. These two figures illustrate the geometry of $W^s(\Gamma^\times)$, which for $L = 100$ is a 'much wider' Möbius band compared to the narrower Möbius band for $L = 8$ shown in Figure 8. In fact, the Möbius in Figures 10 and 11 is too wide to be made from a flat strip of paper; see [31]. This fact highlights the nonlinear and highly curved nature of $W^s(\Gamma^\times)$. Notice in both views of panels (a) and (b), how the boundary of the Möbius band, when followed around from the outside part of $W^s(\Gamma^\times)$ furthest from $\Gamma^\times$, starts to spiral around $W^s(p)$ while transitioning from one side of $\Gamma^\times$ to the other. The rendering in Figure 11(b) illustrates particularly well how the surface $W^s(\Gamma^\times)$ folds very sharply over itself along the bottom-left side of this panel. The development of this sharper and sharper fold on $W^s(\Gamma^\times)$ is an integral part of the process of making an increasingly wider topological Möbius band. Notice that $W^s(\Gamma^\times)$ is actually 'infinitely wide' meaning that it leaves any finite ball

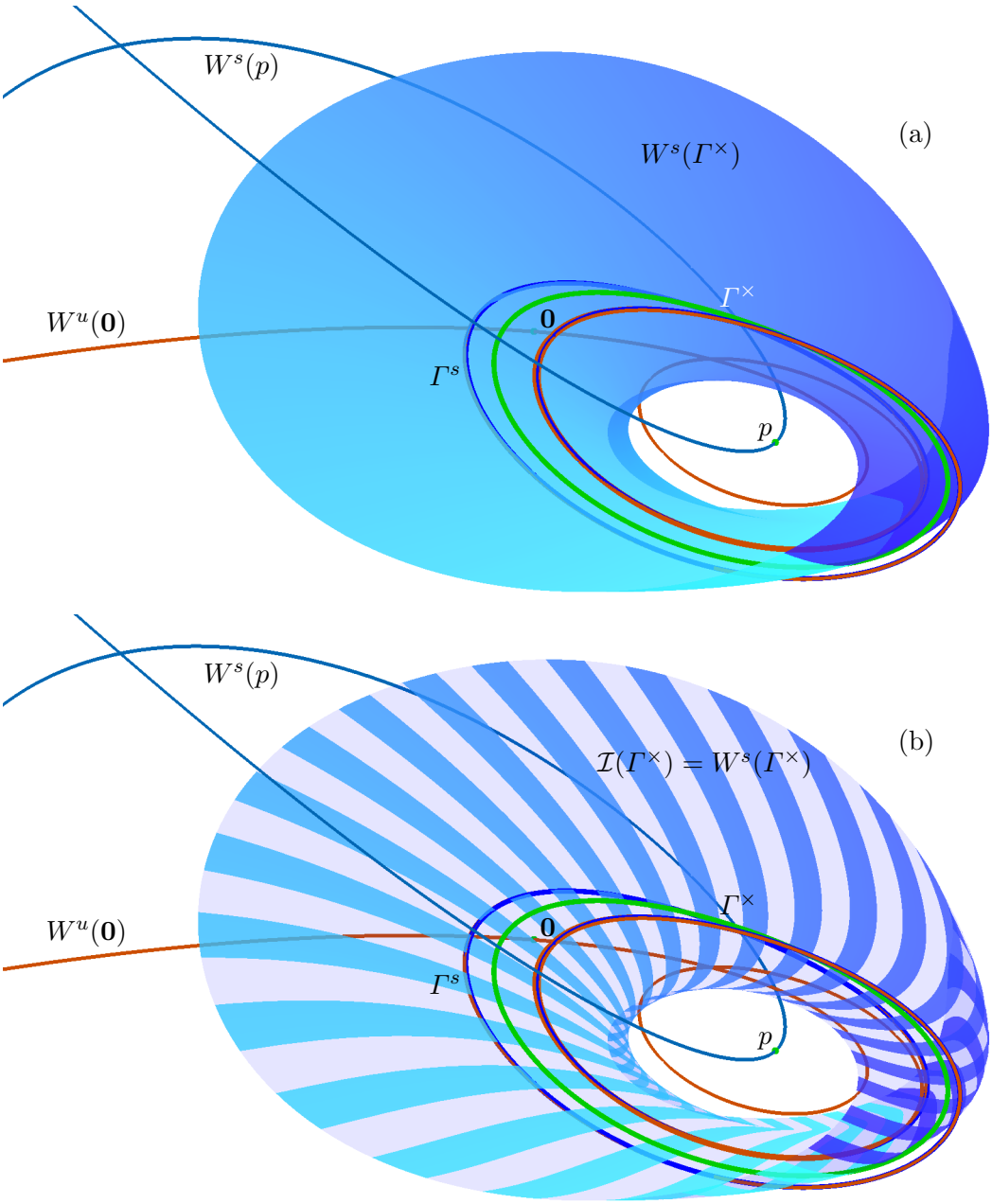

Figure 8: Phase portrait of system (19) near $\Gamma^\times$ (green curve). Shown are the saddle points $\mathbf{0}$ (green dot) and p (green dot), their one-dimensional manifolds $W^u(\mathbf{0})$ (red curve) and $W^s(p)$ (blue curve), the period-doubled periodic orbit Γ^s (blue curve), and the stable manifold $W^s(\Gamma^\times)$ (cyan–blue surface) rendered from 200 computed phase-uniform forward-time isochrons of arclength $L = 8$. In panel (a) the surface $W^s(\Gamma^\times)$ is phase coloured, and in panel (b) it is represented by 50 alternating phase ribbons.

around $\Gamma^\times$ when computed and rendered with isochrons in $\mathcal{I}(\Gamma^\times)$ of suffiently large arclength L. Specifically, and as Figures 10 and 11 illustrate, the Möbius band $W^s(\Gamma^\times)$ approaches infinity along $W^s(p)$.

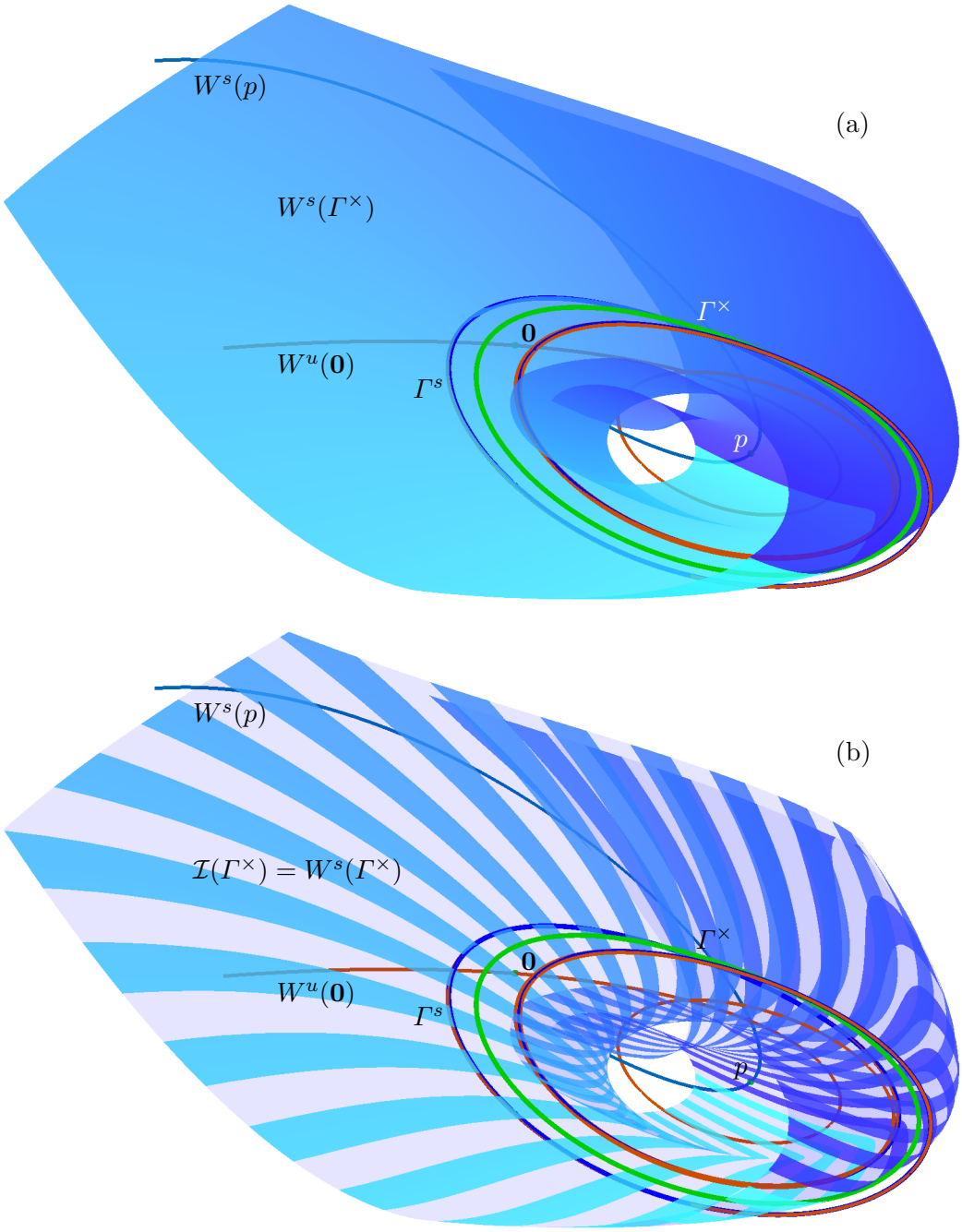

Figure 9: Phase portrait of system (19) in the cube$[0, 5] \times [-4, 4] \times [-5, 4] \subset \mathbb{R}^3$ with invariant objects and presentation as in Figure 8, where $W^s(\Gamma^\times)$ (cyan–blue surface) is now rendered from 200 phase-uniform isochrons of arclength $L = 100$.

6 Conclusions

We presented the isochron manifold algorithm, which computes a representative number of the isochrons that foliate a two-dimensional stable or unstable manifold of a saddle periodic orbit $\Gamma^\times$. This approach is complementary to other methods that represent and compute a two-dimensional global invariant manifold as a one-parameter families of either trajectories or topological circles of constant geodesic distance from $\Gamma^\times$; see [17, 19]. The isochron manifold algorithm provides

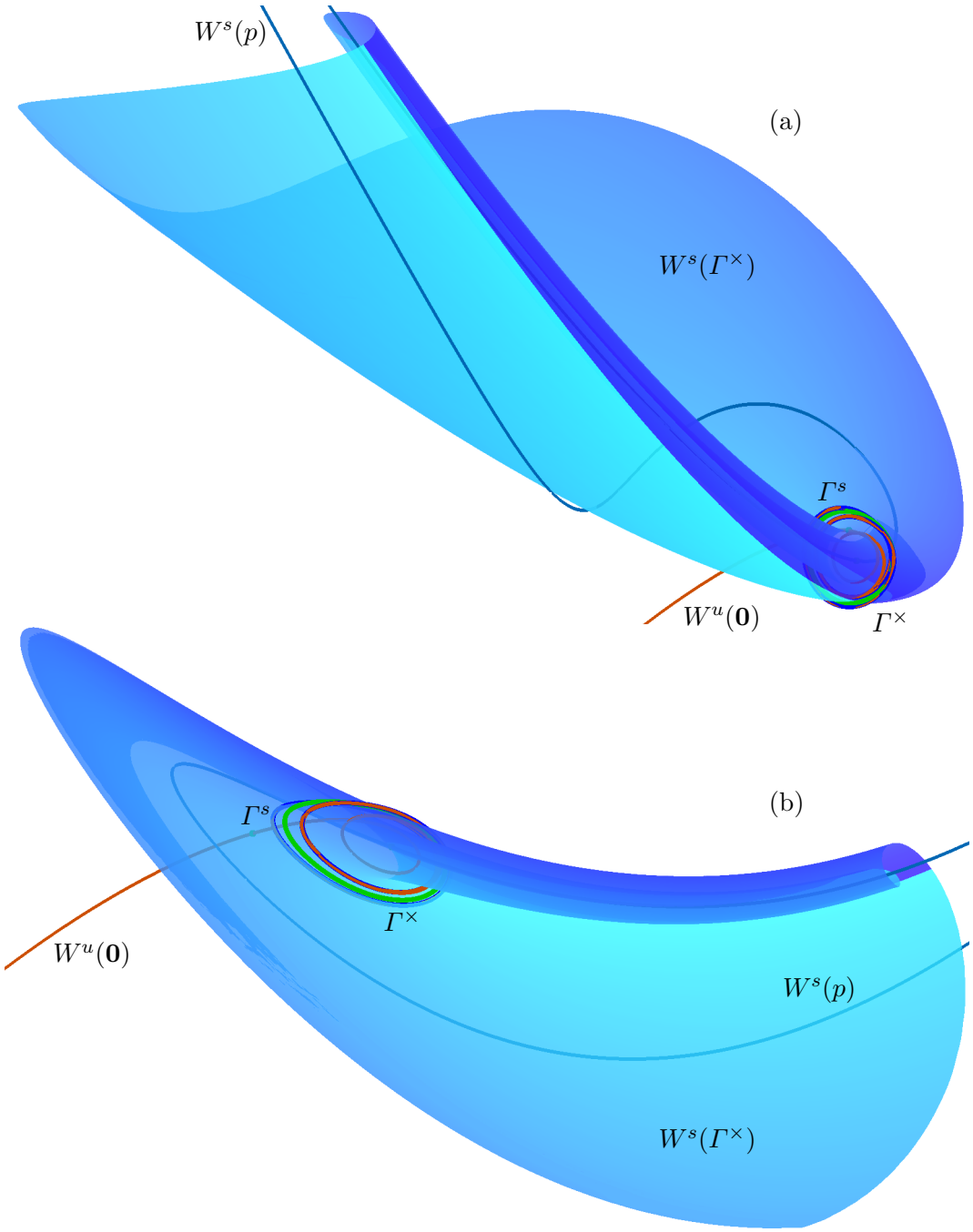

Figure 10: The invariant objects from Figure 9 in a larger region of phase space, shown from two view points in panels (a) and (b), where $W^s(\Gamma^\times)$ is rendered from 200 phase-uniform isochrons of arclength $L = 100$ and coloured by phase.

an efficiently way of finding and then rendering such global invariant surfaces, with the new feature that it emphasises the phase dynamics of trajectories on the manifold as they approach $\Gamma^\times$ in forward or backward time. In particular, note that the isochrons are transverse to $\Gamma^\times$, while trajectories on the invariant manifold become tangent to $\Gamma^\times$.

The isochron manifold algorithm is a relatively straightforward generalisation of the isochron algorithm for one-dimensional isochrons of planar systems. It has been implemented for two-dimensional manifolds in $\mathbb{R}^3$, and the key new ingredient is the construction of a suitable funda-

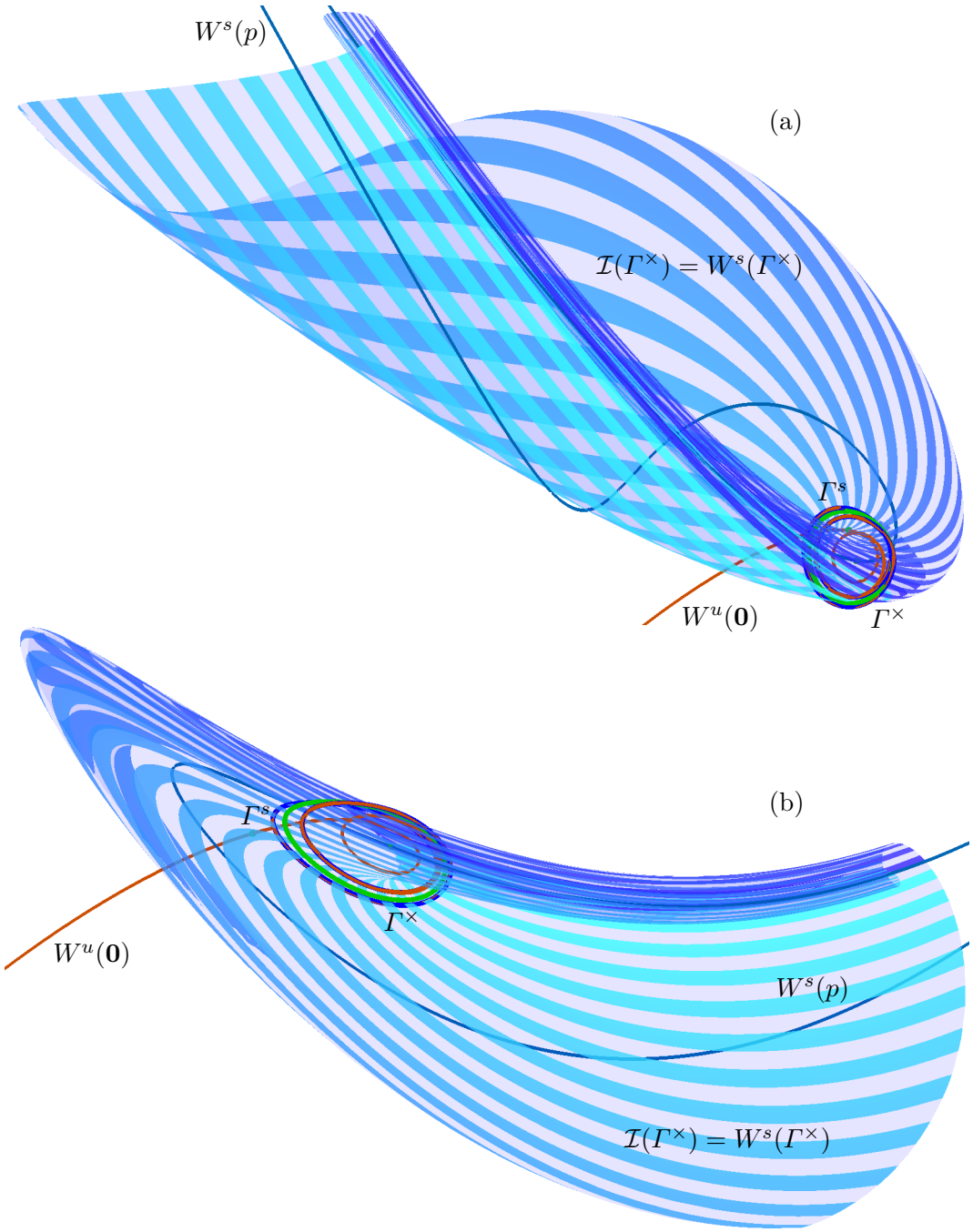

Figure 11: The same objects and views as in Figure 10, where $W^s(\Gamma^\times)$ is now shown as alternating phase ribbons.

mental segment. The set of computed isochrons (each with its own sequence of mesh points) is then turned into a triangulation that represents the invariant manifold as a surface. While the parametrisation by asymptotic phase and arclength along isochrons is natural, simply selecting points on neighbouring isochrons at equal arclength distances generally does not translate into a triangulation of good quality. This is why we generate a triangulation based on smallest Euclidean distance between points on neighbouring isochrons.

The practicality of the isochron manifold algorithm for computing and visualising two-dimensional invariant manifolds of saddle periodic orbits was demonstrated with three examples:

orientable manifolds of periodic orbits in a constructed vector field and in Sandstede's model, as well as a nonorientable manifold of the ζ^3-model. The foliation of an invariant manifold by its isochrons provides phase information, which we showed to be useful when it comes to understanding the geometric properties of two-dimensional stable or unstable manifolds. Colouring the computed part of an invariant manifold according to the phase already gives a good impression of the synchronisation dynamics. Moreover, rendering such a surface as a set of alternating phase ribbons is an effective way to illustrate geometry and phase dynamics at the same time. In particular, the width of ribbons readily allows one to identify regions on the manifold where the flow is fast (greater distances between isochrons) and regions where it is slow (small distances between isochrons).

We remark that the relationship between the curvature of the isochrons and the curvature of the invariant manifold as a surface is an intriguing one. One might expect that regions of high curvature of isochrons naturally correspond to high curvature of the surface, but this is not necessarily the case. As we have seen, a sharp fold of the surface may lead to large curvature of the isochrons when their crossing of the fold is sufficiently transverse; on the other hand, when isochrons effectively run in the direction of such a fold they need not be curved much themselves. Moreover, we have seen that the surface may be rather flat while the isochrons are, nevertheless, strongly curved.

Overall, the isochron manifold algorithm is a new tool that allows one to investigate the synchronisation and phase properties together with the geometric properties of the respective two-dimensional invariant manifold. While our present implementation is for $\mathbb{R}^3$, the computational framework works in an ambient space of any dimension. Moreover, an adapation of the algorithm for computing isochrons of foci in planar systems [14, 23] provides, in the same spirit as for saddle periodic orbits, a BVP setup for finding a two-dimensional stable or unstable manifold of a saddle focus in $\mathbb{R}^n$, associated with a single pair of stable or unstable complex conjugate eigenvalues. Such an implementation and the investigation of relevant examples remain tasks for the future. Finally, we mention that the isochron manifold algorithm presented here is an intermediate step towards computing two-dimensional isochrons that foliate the basin of an attracting or repelling periodic orbits in $\mathbb{R}^3$ — or, similarly, a three-dimensional stable or unstable manifold of a saddle periodic orbit $\Gamma^\times$ in a higher-dimensional space.

Acknowledgements

We thank Peter Langfield for helpful discussion.

References

[1] Aguirre, P., Krauskopf, B., Osinga, H.M.: Global invariant manifolds near homoclinic orbits to a real saddle: (non)orientability and flip bifurcation. SIAM Journal on Applied Dynamical Systems 12(4), 1803–1846 (2013)

[2] Akam, T., Oren, I., Mantoan, L., Ferenczi, E., Kullmann, D.M.: Oscillatory dynamics in the hippocampus support dentate gyrus–CA3 coupling. Nature Neuroscience 15, 763–768 (2012)

[3] Arneodo, A., Coullet, P.H., Spiegel, E.A., Tresser, C.: Asymptotic chaos. Physica D: Nonlinear Phenomena 14(3), 327–347 (1985)

[4] Demongeot, J., Françoise, J.P.: Approximation for limit cycles and their isochrons. Comptes Rendus Biologies 329(12), 967–970 (2006)

[5] Doedel, E.J., Oldeman, B.E., with major contributions from Champneys, A.R., Dercole, F., Fairgrieve, T.F., Kuznetsov, Y.A., Paffenroth, Sandstede, B., Wang, X., Zhang, C.:

AUTO-07P: Continuation and bifurcation software for ordinary differential equations. Manual (2007), http://cmvl.cs.concordia.ca/auto/

[6] England, J.P., Krauskopf, B., Osinga, H.M.: Computing one-dimensional global manifolds of Poincaré maps by continuation. SIAM Journal on Applied Dynamical Systems 4(4), 1008–1041 (2005)

[7] Ermentrout, G.B., Terman, D.H.: Mathematical Foundations of Neuroscience. Springer, New York (2010)

[8] Giraldo, A., Krauskopf, B., Osinga, H.M.: Saddle invariant objects and their global manifolds in a neighborhood of a homoclinic flip bifurcation of case B. SIAM Journal on Applied Dynamical Systems 16(1), 640–686 (2017)

[9] Giraldo, A., Krauskopf, B., Osinga, H.M.: Cascades of global bifurcations and chaos near a homoclinic flip bifurcation: a case study. SIAM Journal on Applied Dynamical Systems 17(4), 2784–2829 (2018)

[10] Guckenheimer, J.: Isochrons and phaseless sets. Journal of Mathematical Biology 1(3), 259–273 (1975)

[11] Guckenheimer, J., Holmes, P.: Nonlinear Oscillations, Dynamical Systems, and Bifurcation of Vector Fields. Springer, New York (1983)

[12] Guillamon, A., Huguet, G.: A computational and geometric approach to phase resetting curves and surfaces. SIAM Journal on Applied Dynamical Systems 8(3), 1005–1042 (2009)

[13] Hannam, J., Krauskopf, B., Osinga, H.M.: Global isochrons of a planar system near a phaseless set with saddle equilibria. The European Physical Journal – Special Topics 225(13–14), 2645–2654 (2016)

[14] Hannam, J., Krauskopf, B., Osinga, H.M.: Isochron foliations and global bifurcations: A case study. Transactions of Mathematics and its Applications 6(2), 1–43 (2022)

[15] Hirsch, M.W., Pugh, C.C., Shub, M.: Invariant manifolds. Bulletin of the American Mathematical Society 76(5), 1015–1019 (1970)

[16] Huguet, G., de la Llave, R.: Computation of limit cycles and their isochrons: Fast algorithms and their convergence. SIAM Journal on Applied Dynamical Systems 12(4), 1763–1802 (2013)

[17] Krauskopf, B., Osinga, H.M.: Computing geodesic level sets on global (un)stable manifolds of vector fields. SIAM Journal on Applied Dynamical Systems 2(4), 546–569 (2003)

[18] Krauskopf, B., Osinga, H.M., Doedel, E.J., Henderson, M.E., Guckenheimer, J., Vladimirsky, A., Dellnitz, M., Junge, O.: A survey of methods for computing (un)stable manifolds of vector fields. International Journal of Bifurcation and Chaos 15(3), 763–791 (2005)

[19] Krauskopf, B., Osinga, H.M., Galán-Vioque, J. (eds.): Numerical Continuation Methods for Dynamical Systems: Path following and boundary value problems. Understanding Complex Systems, Springer, Netherlands (2007)

[20] Krauskopf, B., Rieß, T.: A Lin's method approach to finding and continuing heteroclinic connections involving periodic orbits. Nonlinearity 21(8), 1655–1690 (2008)

[21] Kuznetsov, Y.A.: Elements of Applied Bifurcation Theory. Springer, New York, third edn. (2004)

[22] Langfield, P., Krauskopf, B., Osinga, H.M.: Solving Winfree's puzzle: The isochrons in the FitzHugh–Nagumo model. Chaos: An Interdisciplinary Journal of Nonlinear Science 24(1), 013131 (2014)

[23] Langfield, P., Krauskopf, B., Osinga, H.M.: Forward-time and backward-time isochrons and their interactions. SIAM Journal on Applied Dynamical Systems 14(3), 1418–1453 (2015)

[24] Langfield, P., Krauskopf, B., Osinga, H.M.: A continuation approach to computing phase resetting curves. In: Junge, O., Schütze, O., Froyland, G., Ober-Blöbaum, S., Padberg-Gehle, K. (eds.) Advances in Dynamics, Optimization and Computation: A volume dedicated to Michael Dellnitz on the occasion of his 60^{th} birthday, pp. 3–30. Springer (2020)

[25] Massarwi, F., Gotsman, C., Elber, G.: Paper-craft from 3D polygonal models using generalized cylinders. Computer Aided Geometric Design 25(8), 576–591 (2008)

[26] Oldeman, B.E., Krauskopf, B., Champneys, A.R.: Numerical unfoldings of codimension-three resonant homoclinic flip bifurcations. Nonlinearity 14(3), 597–621 (2001)

[27] Osinga, H.M.: Nonorientable manifolds in three-dimensional vector fields. International Journal of Bifurcation and Chaos 13(3), 553–570 (2003)

[28] Osinga, H.M., Moehlis, J.: Continuation-based computation of global isochrons. SIAM Journal on Applied Dynamical Systems 9(4), 1201–1228 (2010)

[29] Sandstede, B.: Constructing dynamical systems having homoclinic bifurcation points of codimension two. Journal of Dynamics and Differential Equations 9(2), 269–288 (1997)

[30] Sherwood, W.E., Guckenheimer, J.: Dissecting the phase response of a model bursting neuron. SIAM Journal on Applied Dynamical Systems 9(3), 659–703 (2010)

[31] Starostin, E.L., van der Heijden, G.H.M.: The shape of a Möbius strip. Nature Materials 6, 563–567 (2007)

[32] Strogatz, S.H.: Nonlinear Dynamics and Chaos: With Applications to Physics, Biology, Chemistry, and Engineering. CRC Press, Boca Raton, second edn. (2015)

[33] Şuvak, Ö., Demir, A.: Quadratic approximations for the isochrons of oscillators: A general theory, advanced numerical methods, and accurate phase computations. IEEE Transactions on Computer-Aided Design of Integrated Circuits and Systems 29(9), 1215–1228 (2010)

[34] Takeshita, D., Feres, R.: Higher order approximation of isochrons. Nonlinearity 26(6), 1303–1323 (2010)

[35] Wang, C.C.L., Tang, K.: Optimal boundary triangulations of an interpolating ruled surface. Journal of Computing and Information Science in Engineering 5(4), 291–301 (Feb 2005)

[36] Winfree, A.T.: Biological rhythms and the behavior of populations of coupled oscillators. Theoretical Biology 16(1), 15–42 (1967)

[37] Winfree, A.T.: Patterns of phase compromise in biological cycles. Journal of Mathematical Biology 1(1), 73–93 (1974)

[38] Winfree, A.T.: The Geometry of Biological Time. No. 12 in Interdisciplinary Applied Mathematics, Springer, New York, second edn. (2001)